bioRxiv preprint doi: https://doi.org/10.1101/748988; this version posted August 29, 2019. The copyright holder for this preprint (which was not certified by peer review) is the author/funder, who has granted bioRxiv a license to display the preprint in perpetuity. It is made available under aCC-BY-NC-ND 4.0 International license.

Sag currents are a major contributor to human pyramidal cell intrinsic differences across cortical layers and between individuals

Homeira Moradi Chameh[1], Lihua Wang[1], Scott Rich[1], Liang Zhang[2,9], Peter L. Carlen[2,9], Shreejoy J. Tripathy[3,4,5]*, Taufik A. Valiante.[1,5,6,7,8]*

[1] *Krembil Research Institute, Division of Clinical and Computational Neuroscience*
[2] *Department of Physiology, University of Toronto*
[3] *Krembil Centre for Neuroinformatics, Centre for Addiction and Mental Health*
[4] *Department of Psychiatry, University of Toronto.*
[5] *Institute of Medical Sciences, University of Toronto.*
[6] *Department of Surgery, Division of Neurosurgery, University of Toronto*
[7] *Institute of Biomaterials and Biomedical Engineering, University of Toronto*
[8] *Electrical and Computer Engineering, University of Toronto*
[9] *Krembil Research Institute, Division of Experimental and Translational Neuroscience*
**Denotes equal contribution*

Abstract

In the human neocortex, coherent theta oscillations between superficial and deep cortical layers are driven by deep layer neurons, suggesting distinct intrinsic electrophysiological properties of neurons across cortical layers. Here, we used in vitro whole-cell recordings to characterize pyramidal cells in layer 2/3 (L2/3) and layer 5 (L5) of the human neocortex. We found that human L5 pyramidal cells were more excitable and were endowed with a more prominent sag voltage and larger I_h currents relative to L2/3 neurons, that were abolished through direct pharmacological blockade. Although no peak in subthreshold resonance was observed for either L2/3 or L5 cells, we found that L5 neurons demonstrated greater spiking gain at low frequencies. Integrating patient-level demographic features revealed larger sag amplitudes in pyramidal cells recorded from older patients. These data suggest that sag is prominently expressed in L5 pyramidal cells and is a dynamic feature of human cortical microcircuits.

bioRxiv preprint doi: https://doi.org/10.1101/748988; this version posted August 29, 2019. The copyright holder for this preprint (which was not certified by peer review) is the author/funder, who has granted bioRxiv a license to display the preprint in perpetuity. It is made available under aCC-BY-NC-ND 4.0 International license.

1. Introduction

Comparative studies between human and rodent cortical neuronal physiology have revealed unique human cortical neuronal and microcircuit properties. At the cellular level, human neurons have been shown to have unique morphological properties (Mohan, Verhoog et al. 2015), reduced membrane capacitances (Eyal, Verhoog et al. 2016), increased dendritic compartmentalization in L5 pyramidal cells (Beaulieu-Laroche, Toloza et al. 2018), higher h-channel densities in L3 versus L2 pyramidal cells (Kalmbach, Buchin et al. 2018), and a wholly unique inter-neuronal cell type (Boldog, Bakken et al. 2018). At the microcircuit level, human neocortical circuits demonstrate unique reverberant activity (Molnár, Oláh et al. 2008), different short-term plasticity rules as compared to rodents (Silva, Verhoog et al. 2010), and coherent oscillations between superficial and deep cortical layers (Florez, McGinn et al. 2013). At the person level, correlations between patient IQ and cellular features of human L3 pyramidal cells have been demonstrated, namely, action potential width and the length and complexity of dendritic arbors (Goriounova, Heyer et al. 2018).

Although understanding the unique biophysical and synaptic properties of neurons remains an important endeavor, computational models and mathematical formulations of neurons and circuits are essential for describing and explaining mesoscopic level collective dynamics such as oscillations (Skinner 2012, Womelsdorf, Ardid et al. 2014, Markram, Muller et al. 2015). Indeed it has been recently posited that "a set of ***brain simulators*** based on ***neuron models*** at different levels of biological detail" are needed in order to "allow for systematic refinement of candidate network models by comparison with ***experiments***..."(Einevoll, Destexhe et al. 2019). By extension, to create simulations of the human brain and cortical microcircuit, we need neuronal models derived from direct experiments. Thus as we explore what is uniquely human about the human brain, for example to tackle the increasing societal burden of neurological and neuropsychiatric conditions (Ruzzo and Geschwind 2016, Vigo, Kestel et al. 2019), infusing computational models with human derived micro- and mesoscopic cellular and circuit properties will be critically important.

In this context, our previous experiments in human cortical slices have demonstrated that spontaneous theta-like activity, the most ubiquitous oscillatory frequency in the human brain (Groppe, Bickel et al. 2013), can be induced by application of cholinergic and glutamatergic agonists (Florez, McGinn et al. 2013). We observed theta oscillations that were coherent between cortical laminae, with the deep layer leading in phase relative to the superficial layer (Florez, McGinn et al. 2013). We also observed robust cross-frequency coupling between theta and high-gamma activity that was modulated with the strength of synchrony between cortical laminae (McGinn and Valiante 2014) – "so called coordination though coherent phase–amplitude coupling"(von Nicolai, Engler et al. 2014). Given the role of intrinsic electrophysiological properties in the generation of theta and our previous findings that deep layer theta leads superficial layer theta in phase, we reasoned that deep layer neurons in the human neocortex are likely endowed with distinct biophysical properties that enable them to "drive" activity in the superficial layers.

One of the candidate membrane currents thought to contribute to theta oscillations is the hyperpolarization activated cation current or h-current (I_h) (Hu, Vervaeke et al. 2002, Das and Narayanan 2017, Kalmbach, Buchin et al. 2018). This current is important for oscillations and pacemaking activity in a myriad of cell types, ranging from thalamic and hippocampal neurons to cardiac pacemaker cells (Neuhoff, Neu et al. 2002, Gastrein, Gasselin et al. 2011). Consistent with its role in contributing to resonant activity, in a recent study in the human neocortex, Kalmbach et al 2018 demonstrated more prominent sag in deep Layer 3 versus more superficial Layer 2 cells, and further, that I_h appeared necessary for the theta frequency resonance observed in the L3 neurons (Kalmbach, Buchin et al. 2018).

bioRxiv preprint doi: https://doi.org/10.1101/748988; this version posted August 29, 2019. The copyright holder for this preprint (which was not certified by peer review) is the author/funder, who has granted bioRxiv a license to display the preprint in perpetuity. It is made available under aCC-BY-NC-ND 4.0 International license.

Based on our previous findings demonstrating that deep layer theta activity appears to drive superficial activity, we hypothesized that intrinsic pyramidal cell properties would differ between deep versus superficial layers. We used whole-cell recordings to characterize superficial and deep layer cortical neurons, focusing in particular on the amplitude and kinetics of I_h current or sag voltage. In addition to key biophysical differences favoring greater excitability in human L5 vs. L2/3 pyramidal cells, we found that L5 demonstrated significantly larger sag voltage amplitudes relative to L2/3 pyramidal cells. Though we did not see strong evidence for theta resonance in either L5 or L2/3 cells, we observed that L5 cells are better able to track suprathreshold inputs delivered at theta frequencies. Lastly, to better understand the observed cell-to-cell variability in sag amplitudes, we correlated these data with patient-specific demographic features, including patient age. We found that sag amplitudes tended to increase over the human lifetime, and critically, we were able to externally replicate these findings in an additional cohort of human patients characterized by the Allen Institute.

2. Materials and Methods

2.1. Human brain slice preparation

Written informed consent was obtained from all study participants as stated in the research protocol. In accordance with the Declaration of Helsinki, approval for this study was received by the University Health Network Research Ethics board. A total of fifty one patients, age ranging between 19 to 63 (Mean age: 36 ± 2), underwent a standard anterior temporal lobectomy (ATL) (Mansouri, Fallah et al. 2012) or tumor resection from the frontal or temporal lobe (Kostopoulos, Drapeau et al. 1989, Köhling and Avoli 2006) under general anesthesia using volatile anesthetics.

The surgery involved resecting the first 4.5 cm of neocortex using sharp dissection and local cooling with ∼4 °C TissueSol®. Immediately following surgical resection, the cortical block was submerged in an ice-cold (~4°C) cutting solution that was continuously bubbled with 95% O_2-5% CO_2 containing (in mM) sucrose 248, KCl 2, $MgSO_4.7H_2O$ 3, $CaCl_2.2H_2O$ 1, $NaHCO_3$ 26, $NaH_2PO_4.H_2O$ 1.25, D-glucose 10. The osmolarity was adjusted to 300-305 mOsm. The total duration, including slicing and transportation, was kept to a maximum of 20 minutes (Köhling and Avoli 2006). Transverse brain slices (400 µm) were obtained using a vibratome (Leica 1200 V) in cutting solution. Tissue slicing was performed perpendicular to the pial surface to ensure that pyramidal cell dendrites were minimally truncated (Kostopoulos, Drapeau et al. 1989, Kalmbach, Buchin et al. 2018). The cutting solution was the same as used for transport of tissue from operation room to the laboratory. After sectioning, the slices were incubated for 30 min at 34 °C in standard artificial cerebrospinal fluid (aCSF) (in mM): NaCl 123, KCl 4, $CaCl_2.2H_2O$ 1, $MgSO_4.7H_2O$ 1, $NaHCO_3$ 25, $NaH_2PO_4.H_2O$ 1.2, and D-glucose 10, pH 7.40. All aCSF and cutting solutions were continuously bubbled with carbogen gas (95% O_2-5% CO_2) and had an osmolarity of 300-305 mOsm. Following this incubation, the slices were maintained in standard aCSF at 22–23 °C for at least 1 h, until they were individually transferred to a submerged recording chamber.

For a subset of experiments designed to assess frequency gain dependent, slices were prepared using the NMDG protective recovery method (Ting, Daigle et al. 2014). The slicing and transport solution was composed of (in mM): NMDG 92, KCl 2.5, NaH_2PO_4 1.2, $NaH_2PO_4.H_2O$ 30, HEPES 20, Glucose 25, Thiourea 2, Na L-ascorbate 5, Na-Pyruvate 3, $CaCl_2.2H_2O$ 0.5, and $MgSO_4.7H_2O$ 10. The pH of NMDG solution was adjusted to 7.3-7.4 using hydrochloric acid and the osmolarity was 300-305 mOsm. Before transport and slicing, the NMDG solution was carbogenated for 15 min and chilled to 2-4 °C. After slices were cut (as described above), they were transferred to a recovery chamber filled with 32-34 °C NMDG solution continuously bubbled with 95% O_2 5% CO_2. After 12 minutes, the slices were transferred to an incubation solution containing (in mM): NaCl 92, KCl 2.5, $NaH_2PO_4.H_2O$ 1.2, $NaHCO_3$ 30, HEPES 20, Glucose 25, Thiourea 2, Na L-ascorbate 5, Na-Pyruvate 3, $CaCl_2.2H_2O$ 2, and $MgSO_4.7H_2O$ 2. The solution was continuously

bioRxiv preprint doi: https://doi.org/10.1101/748988; this version posted August 29, 2019. The copyright holder for this preprint (which was not certified by peer review) is the author/funder, who has granted bioRxiv a license to display the preprint in perpetuity. It is made available under aCC-BY-NC-ND 4.0 International license.

bubbled with 95% O_2 -5% CO_2. After a 1 hour incubation at room temperature, slices were transferred to a recording chamber continuously perfused with aCSF containing (in mM): NaCl 126, KCl 2.5, $NaH_2PO_4.H_2O$ 1.25, $NaHCO_3$ 26, Glucose 12.6, $CaCl.H_2O$ 2, and $MgSO_4.7H_20$ 1.

2.2. Electrophysiology recordings

For recordings, slices were transferred to a recording chamber mounted on a fixed-stage upright microscope (Olympus $BX_{51}WI$ upright microscope; Olympus Optical Co., NY, USA and Axioskop 2 FS MOT; Carl Zeiss, Germany), and were continually perfused at 8 ml/min with standard aCSF at 32-34 ^{o}C. Cortical neurons were visualized using an IR-CCD camera (IR-1000, MTI, USA) with a 40x water immersion objective lens. Using the IR-DIC microscope, the boundary between layer 1 and 2 was easily distinguishable in terms of cell density. Below layer 2 the sparser area of cells (L3) were followed by a tight band of densely packed L4 cells. L4 was followed by a decrease in cell density (L5). In general, we did not annotate differently cells recorded from layer 2 versus those recorded from layer 3, except when mentioned otherwise.

Patch pipettes (3-6 MΩ resistance) were pulled from standard borosilicate glass pipettes (thin-wall borosilicate tubes with filaments, World Precision Instruments, Sarasota, FL, USA) using a vertical puller (PC-10, Narishige). Pipettes were filled with intracellular solution containing (in mM): K-gluconate 135; NaCl 10; HEPES 10; $MgCl_2$ 1; Na_2ATP 2; GTP 0.3, pH adjusted with KOH to 7.4 (290–300 mOsm). In a subset of experiments the pipette solution also contained biocytin (3-5%). Whole-cell patch-clamp recordings were obtained using a Multiclamp 700A amplifier and pClamp 9.2 data acquisition software (Axon instruments, Molecular Devices, USA). Subsequently, electrical signals were digitized at 20 kHz using a 1320X digitizer. The access resistance was monitored throughout the recording (typically between 8-25 MΩ), and cells discarded if access resistance was > 25 MΩ. The liquid junction potential was calculated to be 10.8 mV and was not corrected.

Data were analysed off-line using MATLAB and R software. The resting membrane potential (RMP) was calculated by subtraction of the tip potential occurring when the microelectrode was withdrawn from the neuron. We also calculated the input resistance (R_N) of neurons, described as the slope of the regression line fitted to the voltage-current curve, by measuring the average response to the injection of hyperpolarizing current pulses (600 ms duration, 50-400 pA). The membrane time constant (τ_m) was calculated using a single-exponential fit of the membrane potential response to a small hyperpolarizing pulse. Voltage sag amplitude in response to hyperpolarizing current pulses, was determined as the voltage difference between the peak hyperpolarization and the steady-state membrane potential. The sag ratio was calculated as the difference between minimum value and the steady state divided by peak deflection during hyperpolarization current injection. The rebound depolarization amplitude was calculated as the difference between the steady state potential and the maximum depolarization potential. We also observed the presence or absence of rebound spiking following the injection of hyperpolarization current steps. The I_h blocker ZD7288 (10 μM, Sigma Aldrich) was applied to confirm pharmacological evidence for I_h in L2/3 and L5 pyramidal cells.

Suprathreshold current injection was used to characterize the AP amplitude and half width of pyramidal neurons. Action potential amplitude was measured as the difference between the threshold potential and the peak potential of the spike waveform. Half-width was measured as the width at half-maximal spike amplitude.

The frequency-current relationship (the f-*I* curve) was computed following the injection of depolarization current (50-400 pA, 600ms). The adaptation index was calculated by dividing the mean of the three last inter-spike intervals with the mean of the three first inter-spike intervals following positive current steps (600 ms duration, 50-400 pA).

bioRxiv preprint doi: https://doi.org/10.1101/748988; this version posted August 29, 2019. The copyright holder for this preprint (which was not certified by peer review) is the author/funder, who has granted bioRxiv a license to display the preprint in perpetuity. It is made available under aCC-BY-NC-ND 4.0 International license.

2.3. Characterisation of I_h and I_h tail currents

To characterize the I_h current, 600 ms-long voltage-clamp steps were used in -10mV increments, down to -140mV from a holding potential of -60mV. In order to measure I_h current amplitude, the difference between the steady state at the end of the holding potential and the maximum current was determined. The I_h tail current was quantified as the difference between peak amplitude of residual current at the end of each holding potential and the steady state current from holding potentials of -140 to -60 mV. A single or double-exponential model, fitted to the various currents recorded, was used to calculate the time constants of I_h current in order to determine the kinetics of I_h. The kinetics of I_h tail current activation were measured by fitting the onset of I_h tail current with a single exponential curve using Clampfit 10.7 (Molecular devices). To measure the voltage sensitivity of I_h current in L2/3 and L5 pyramidal cells, the membrane potential evoking half-maximal activation of I_h (V_{50}) was obtained by fitting the I_h current activation to a Boltzmann sigmoid function using Graphpad 6 (Graphpad, San Diego, CA, USA).

In experiments to quantify I_h, currents the sodium channel blocker tetrodotoxin (1 µM; Alomone Labs) to block voltage gated sodium currents, $CoCl_2$ (2mM; Sigma-Aldrich) to block voltage-sensitive calcium currents, and $BaCl_2$ (1mM; Sigma-Aldrich) to block inwardly rectifying potassium current were added to the bath solution.

2.4. Resonance and spike probability analyses

To assess the subthreshold and suprathreshold resonance properties of L2/3 and L5 pyramidal cells, a frequency modulated sine wave current input (ZAP) was generated ranging from 1 to 20Hz, lasting 20s (Hutcheon, Miura et al. 1996) with a sampling rate of 10kHz. This current waveform was then injected using the custom waveform feature of Clampex 9.2 (Axon Instruments, Molecular devices, USA). The subthreshold current amplitude was adjusted to the maximal current that did not elicit spiking.

For determining subthreshold resonance, only trials without spiking were utilized for analysis. Analyses were performed using in house MATLAB scripts. As described previously (Hutcheon, Miura et al. 1996) the impedance of the cell was obtained by dividing the power spectrum of the voltage response by the power spectrum of the injection current. An average of at least 5 trials (maximum 10) was used to compute the impedance of the cell. To average across cells, the impedance of each cell was averaged. To compare between cell types and between conditions, the *p* value at each frequency was obtained by performing the Wilcoxon rank sum test (`ranksum.m`) using cell impedances (not individual trial impedances), with significance obtained after false-discovery rate correction (Benjamini and Hochberg 1995).

Spiking probability was computed using suprathreshold current stimulation. The suprathreshold current was set by gradually increasing in the amplitude of the ZAP function input by adjusting the gain of the stimulus until the first spike was elicited. The input current was then adjusted to obtain at least one spike at the lowest frequency. Ten traces per cell were utilized to obtain the probability of spiking as a function of frequency. Since the instantaneous frequency is known from the current input, each action potential could be assigned a frequency at which it occurred. To create the spike probability density function for each cell type, the frequencies at which individual spikes occurred were pooled, a histogram generated and divided by the total number of spikes. To compare spike probability density functions between cell types the distributions were compared using a two-sample Kolmogorov-Smirnov test (`kstest2.m`).

bioRxiv preprint doi: https://doi.org/10.1101/748988; this version posted August 29, 2019. The copyright holder for this preprint (which was not certified by peer review) is the author/funder, who has granted bioRxiv a license to display the preprint in perpetuity. It is made available under aCC-BY-NC-ND 4.0 International license.

2.5. Frequency Dependent Gain

Following a similar methodology of (Higgs and Spain 2009), frequency dependent gain was computed using 30 trials (inter-trial interval = 20s) of a 2.5s duration current injection stimulus of frozen white noise convolved with a 3ms square function (Galán, Ermentrout et al. 2008). The amplitude, or variance of the current injection stimulus was scaled to elicit spike rates of above 5 Hz the typical firing rate for cortical pyramidal cells (Neske and Connors 2016). In addition to increasing the noise variance, a steady amount of DC current was required (Higgs and Spain 2009) to elicit spiking which was delivered as various amplitude steps added to the noisy current input. Peaks detected in the voltage time series with overshoot greater than 0 mV were taken to be the occurrence of an action potential. The time varying firing rate *r(t)* was given by:

$$r(t) = \begin{Bmatrix} \frac{1}{\Delta t} & \textit{where spike detected} \\ 0 & \textit{Where no spike detected} \end{Bmatrix}$$

with σ= 1/f, so that the spectral estimates are not dominated by noise. The gain (G(f)) and the phase ($\varphi(f)$).

$$G(f) = \frac{|C_{sr}(f)|}{|C_{ss}(f)|}$$

$$\varphi(f) = atan\frac{[Im[C_{sr}(f)]]}{[Re[C_{sr}(f)]]}$$

Where *Re* and *Im* refer to the real and imaginary parts of each Fourier component. φ(f) was then correct using the peak time (τ_{delay}) of $c_{sr}(\tau)$ (Higgs and Spain 2009).

For statistical testing, individual gains or G(f)s for each cell (30 trials/cell) from cells with spike rates above 5Hz were pooled for each cell type. To compare between cell types, Mann-Whitney U (`ranksum.m`) was used to obtain a *p*-value at each frequency (2-100Hz in 0.2Hz steps). The *p*-values were false discovery rate corrected with an alpha = 0.01 (Benjamini and Hochberg 1995).

2.6. Histological methods

During electrophysiological recording, biocytin (3-5 mg/ml) was allowed to diffuse into the patched neuron; after 20-45 min, the electrodes were slowly retracted under visual guidance to maintain the quality of the seal and staining. The slices were left for another 10-15 min in the recording chamber to washout excess biocytin from extracellular space, then transferred to 4% paraformaldehyde and kept at 4°C for 24 hours.

Subsequently, the slices were washed and transferred into PBS solution (0.1 mM). To reveal biocytin, slices were incubated in blocking serum (0.5 % Bovine serum albumin (BSA), 0.5 % milk powder) and 0.1% Triton X-100 in PBS for 1 hour at room temperature. Finally, slices were incubated with streptavidin-conjugated Alexa Fluor 568 (1:300) overnight at 4°C. Then slices were rinsed with PBS and mounted on the slide using moviol (Sigma-Aldrich). Imaging was done using a Zeiss LSM710 Multiphone microscope. Reconstructions were performed using IMARIS software (Bitplane, Oxford instrument company).

bioRxiv preprint doi: https://doi.org/10.1101/748988; this version posted August 29, 2019. The copyright holder for this preprint (which was not certified by peer review) is the author/funder, who has granted bioRxiv a license to display the preprint in perpetuity. It is made available under aCC-BY-NC-ND 4.0 International license.

2.7. Statistical analyses

All data were recorded using pClamp 9.2 (Axon Instruments) and analysed using MATLAB and Clampfit 10.7. Statistical analyses and plotting were performed using GraphPad Prism 6. Data are presented in the text as mean ± SD. Unless stated otherwise, a standard threshold of $p<0.05$ was used to report statistically significant differences. Student's *t*-tests were paired or unpaired, whenever deemed appropriate.

To evaluate the presence of correlations between electrophysiological variables and patient demographic variables, we used a mixed effects modeling approach, implemented in R using lme4 (Bates, Mächler et al. 2014). Specifically, we modeled age as a fixed effect and patient ID as a random effect, i.e., ephys_prop ~ age + (1|subject_id). To evaluate the statistical significance of the demographic term, we fit a second model with the random effect only and used an ANOVA to evaluate the difference between the two models. To calculate correlation coefficients from mixed effects models for fixed effects terms (like age), we used the MuMIn R package to calculate the R squared values associated with our fixed effects (i.e., the marginal effect) and calculated the square root of this to obtain a correlation coefficient (Anderson and Burnham 2004).

3. Results

Whole-cell patch clamp recordings were made from human neocortical neurons located in L2/3 and L5 within acute brain slices collected from 51 patients. Tissues were obtained from patients who underwent resective surgery for pharmacologically intractable epilepsy or tumor removal (a summary table with patient details shown in Supplemental Table 1). We note that in general, we did not annotate our L2/3 pyramidal cells as specifically belonging to either L2 or L3, as the majority of these data were collected prior to publication of a recent paper illustrating divergent electrophysiological and morphological features of these cells in the human neocortex(Kalmbach, Buchin et al. 2018).

bioRxiv preprint doi: https://doi.org/10.1101/748988; this version posted August 29, 2019. The copyright holder for this preprint (which was not certified by peer review) is the author/funder, who has granted bioRxiv a license to display the preprint in perpetuity. It is made available under aCC-BY-NC-ND 4.0 International license.

Table 1: Demographic data (for a subset of 40 patients where such information was available)

Age (Years)	Sex	Years of seizure history	Diagnosis	Antiepileptic drugs	Resection location
39	F	11	Tumor	LSC, LRZ, LEV,	Right-ATL
58	F	8	Tumor	CBZ	Left-FL
57	M	45	Epilepsy	LSC, CZP, CBZ	Right-ATL
27	M	11	Epilepsy	LSC, LRZ, CLB	Right-ATL
24	M	8	Epilepsy	LEV, LTG	Right-ATL
25	M	12	Epilepsy	CBZ, LSC	Right-ATL
33	F	4	Epilepsy	LEV	Left-FL
33	M	14	Epilepsy	PHN, LEV	Right-FL
22	M	6	Epilepsy	PHN, CBZ, LTG	Left-ATL
21	M	2	Epilepsy	DR, CLB, MJ	Parietal lobe
22	M	12	Epilepsy	PHN, LRZ	Right-ATL
23	F	23	Epilepsy	CBZ, LEV, LSC	Right-FL
53	F	43	Epilepsy	CBZ, LSC, LEV	Left-ATL
37	F	2	Tumor	GPN, LSC, LEV, CLB, LRZ	Right-FL
47	F	4	Epilepsy	CBZ, CLB	Left-ATL
52	M	13	Epilepsy	CBZ, CLB	Left-ATL
50	F	26	Epilepsy	PHN, LTG	Right-ATL
36	F	34	Epilepsy	LSC, CBZ	Left-ATL
40	M	29	Epilepsy	LEV	Right-ATL
25	F	10	Epilepsy	CBZ, LSC, LEV	Right-ATL
52	M	27	Epilepsy	LSC, LRZ	Left-ATL
21	M	11	Epilepsy	LTG, CBZ	Left-ATL
63	M	0.1	Tumor	PHN	Right-Parietal
42	M	22	Epilepsy	CBZ	Right-FL
22	F	19	Epilepsy	CZP, LTG, LEV, CLB	Right-ATL
25	F	22	Epilepsy	LSC, CLB, LTG	Right-FL
24	F	3	Tumor	LEV	Left-ATL
53	M	9	Epilepsy	LEV	Left-ATL
45	F	20	Epilepsy	LTG	Right-ATL
26	F	25	Epilepsy	CBZ, CLB, LTG	Right-ATL
35	F	14	Epilepsy	LRZ, DR, PHN	Left-ATL
24	M	6	Epilepsy	LSC, LRZ, MJ	Right-ATL
53	F	51	Epilepsy	LSC, CLB	Left-ATL
44	F	3	Epilepsy	LTG	Left-ATL
25	M	14	Epilepsy	CBZ	Right-ATL
19	F	15	Epilepsy	PB, CLB, GPN, RFM	Right-ATL
30	M	12	Epilepsy	PHN	Left-ATL
26	M	5	Epilepsy	CBZ, DR	Right-ATL
28	M	13	Epilepsy	CLB, MJ	Left-ATL
52	F	6	Epilepsy	LTG, LEF	Left-ATL

CBZ, Carbamazepine; CLB, Clobazam; CZP, Clonazepam; DR, Divalproex; GPN, Gabapentin; LEV, Levetiracetam; LRZ, Lorazepam; LSC, Lacosamide; LTG, Lamotrigine; MJ, Marijuana; PB, Phenobarbital; PHN, Phenytoin; RFM, Rufinamide; LEF, Leflunomide.

In order to confirm the successful targeting of L2/3 and L5 pyramidal neurons, a subset of neurons were stained with biocytin. Figure 1A shows an example of recordings of L2/3 and L5 pyramidal cells with corresponding 3D reconstructions. We observed that the apical dendrites of L2/3 pyramidal cells often reached layer 1 and displayed more complex dendritic branching than L5 pyramidal cells. These qualitative findings are consistent with a recent detailed demonstration of the distinct cellular morphologies of human cortical cells as a function of the cortical lamina (Mohan, Verhoog et al. 2015, Kalmbach, Buchin et al. 2018),

bioRxiv preprint doi: https://doi.org/10.1101/748988; this version posted August 29, 2019. The copyright holder for this preprint (which was not certified by peer review) is the author/funder, who has granted bioRxiv a license to display the preprint in perpetuity. It is made available under aCC-BY-NC-ND 4.0 International license.

compared to mouse neurons. Based on these morphological features alone we expect that L5 cells should have distinct active and passive properties as compared to L2/3 pyramidal cells (Migliore and Shepherd 2005). To explore this possibility, we performed current clamp recordings to characterize passive and active membrane properties.

3.1. Passive membrane properties of pyramidal cells in layers 2/3 and 5

We compared the passive membrane properties (i.e. RMP, input resistance and membrane time constant) of human cortical pyramidal neurons in L2/3 and L5 (n = 82 and 147 cells, respectively), determined by injecting hyperpolarizing currents using current-clamp (see Methods). We found that the passive membrane properties differed significantly between pyramidal cells of L2/3 and L5. Comparing L2/3 to L5 pyramidal cells, we found that L5 cells had significantly more depolarized RMP (L2/3: -71 ± 6mV, L5: -68 ± 8mV, $p<0.01$; Figure 1B) and had higher input resistances relative to L2/3 cells (L2/3: 68 ± 26 MΩ, L5: 87 ± 38MΩ, $p<0.0001$; Figure1C). L5 pyramidal cells also had significantly slower membrane time constants (τ_m) (L2/3: 19 ± 29 ms, L5: 29 ± 37 ms, $p<0.05$; Figure 1D).

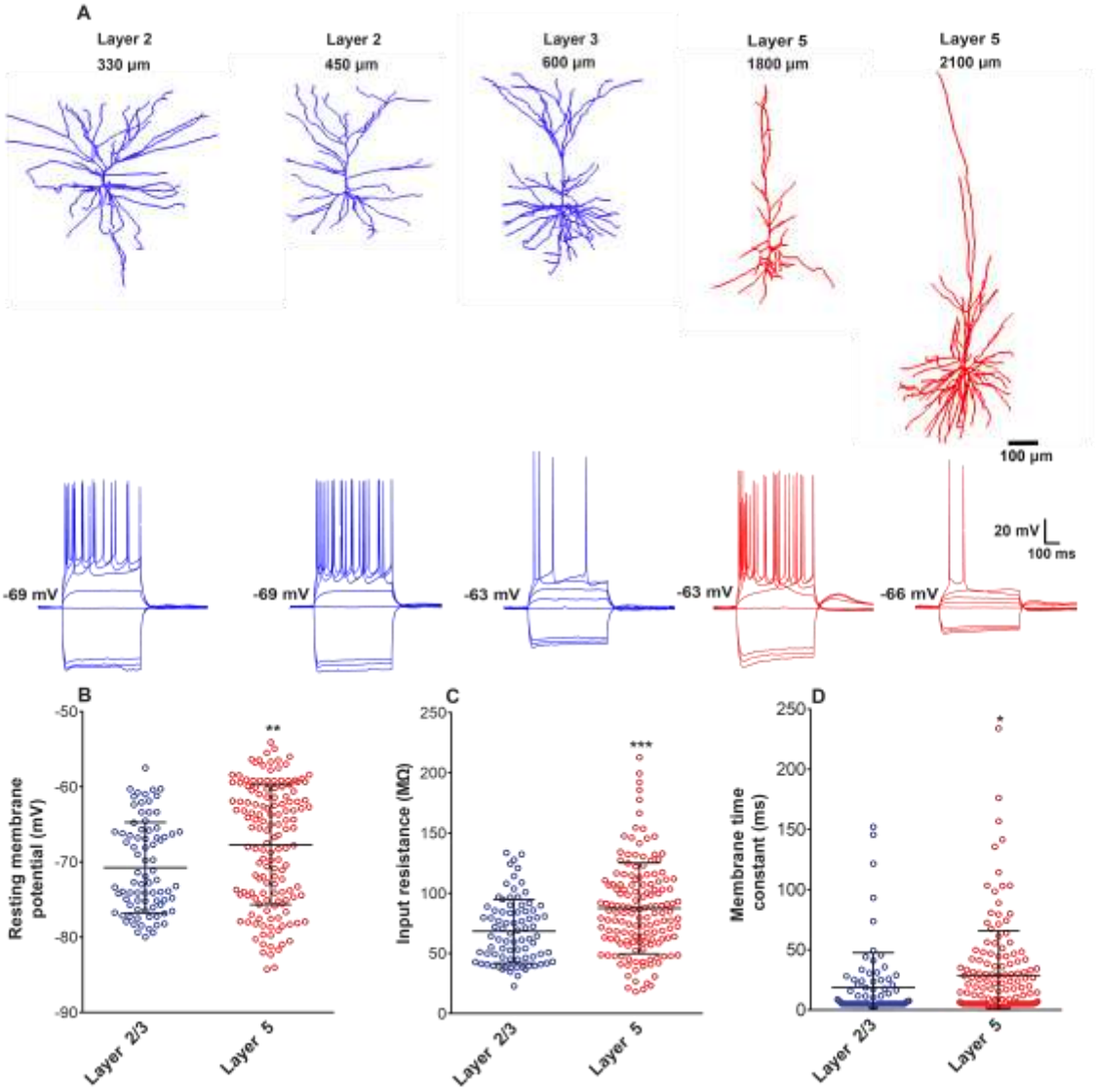

bioRxiv preprint doi: https://doi.org/10.1101/748988; this version posted August 29, 2019. The copyright holder for this preprint (which was not certified by peer review) is the author/funder, who has granted bioRxiv a license to display the preprint in perpetuity. It is made available under aCC-BY-NC-ND 4.0 International license.

Figure 1. L2/3 and L5 pyramidal cells display different passive properties: (A) Example 3D reconstructions and voltage traces L2/3 and L5 pyramidal cells following hyperpolarizing and depolarizing current injection. Cortical layer and distance from pial surface are annotated for each reconstructed cell. **(B)** L5 pyramidal cells are more depolarized at rest than L2/3. **(C)** L5 pyramidal cells have higher input resistances compared to L2/3. **(D)** L5 Pyramidal cells also have significantly slower membrane time constants (τ_m) at rest than L2/3 pyramidal cells. *, **,***, indicate significantly different at P < 0.001, P < 0.05, P < 0.001, respectively. Error bars in B-D denote standard deviations (SD).

3.2. Subthreshold active membrane properties of pyramidal cells in layers 2/3 and 5

We next injected a series of hyperpolarizing currents to assay sag voltage and rebound depolarization and post-inhibitory rebound-evoked spiking in L2/3 and L5 cells (L2/3: n=82, L5: n=147). L5 pyramidal cells had significantly lager sag voltage amplitudes than L2/3 pyramidal cells (L2/3: 1.9 ± 1.3mV, L5: 4.0 ± 2.9mV, p<0.0001; Figures 2A, B, S1). We found similar findings using the dimensionless sag ratio measure, that normalizes for input resistance differences between cells (Figure S2A). In addition, 50% of L5 pyramidal neurons exhibited rebound spiking following the termination of a hyperpolarizing current pulse, whereas no rebound spike was observed in any L2/3 pyramidal cell. The rebound depolarization amplitude was also larger in L5 pyramidal cells in comparison to L2/3 cells (L2/3: 1.9 ± 1.6mV, L5: 4.9 ± 3.5mV, p<0.0001; Figure 2C).

To further characterize the I_h-specific component of membrane sag voltages, in a subset of recordings we bath applied the specific I_h blocker, ZD7288 (10 µm; ZD), with example traces shown in Figure 2D. For both L2/3 (n=9) and L5 (n=12) pyramidal cells, after bath-applying ZD we observed a significant reduction of voltage sag amplitude (L2/3: before 1.7 ± 1.4mV, after 0.18 ± 0.50mV, p<0.01; L5: before 5.6 ± 5.1mV, after 1.1 ± 1.1mV, p<0.01; Figure 2E) and in sag ratio (Figure S2B). Bath applying ZD7288 also significantly reduced the rebound depolarization amplitude (L2/3: before 2.0 ± 2.5 mV, after -1.3 ± 1.3 mV, p<0.01; L5: before 2.5 ± 2.0 mV, after -1.2 ± 1.3mV, p<0.01; Figure 2F). In addition, we observed that the between-cell differences in sag voltages and rebound amplitudes (i.e., the within-group standard deviations) for L2/3 and L5 were markedly reduced after bath application of ZD (Figure 2E, F). These data strongly suggest that non selective voltage-gated cation channels mediating I_h are major contributors to differences between L2/3 and L5 human pyramidal cells.

To further characterize the I_h current in L2/3 and L5 cells, we also we performed whole-cell voltage-clamp experiments. We used pharmacological blockers to specifically isolate I_h (see Methods). We found that injecting hyperpolarizing current steps from -60 to -140 mV produced a slowly activating I_h current (example traces shown in Figure 2G). We found that the amplitudes of the I_h current were significantly smaller in L2/3 neurons compared with L5 (L2/3: n= 6, L5: n= 10; p<0.01 at -140 mV, Figure 2H). Additionally, the amplitude of I_h tail current measured following hyperpolarizing voltage steps was smaller in L2/3 neurons than L5 (L2/3: n= 6 , L5: n= 10, Figure 2I), however, these differences were not statistically significant (p=0.8).

We next assessed the kinetic and voltage activation characteristics of the I_h current in L2/3 and L5 cells. We found that the time course of I_h activation was similar between L2/3 and L5 pyramidal cells (L2/3: n= 6, L5: n= 10, Figure S3; p=0.-6). In addition, the voltage sensitivity of I_h (quantified at the half maximal activation voltage) was similar between L2/3 and L5 neurons (L2/3: n= 6, -96 ± 6 mV, L5: n= 9; -93 ± 2 mV; p<0.05, Figure 2H). These findings suggest that the smaller I_h currents we observe in L2/3 neurons are likely due to lower HCN channel number rather than differences in HCN kinetics. These findings are consistent with recent single-cell transcriptomic-based findings from similar neurons (Kalmbach, Buchin et al. 2018).

bioRxiv preprint doi: https://doi.org/10.1101/748988; this version posted August 29, 2019. The copyright holder for this preprint (which was not certified by peer review) is the author/funder, who has granted bioRxiv a license to display the preprint in perpetuity. It is made available under aCC-BY-NC-ND 4.0 International license.

bioRxiv preprint doi: https://doi.org/10.1101/748988; this version posted August 29, 2019. The copyright holder for this preprint (which was not certified by peer review) is the author/funder, who has granted bioRxiv a license to display the preprint in perpetuity. It is made available under aCC-BY-NC-ND 4.0 International license.

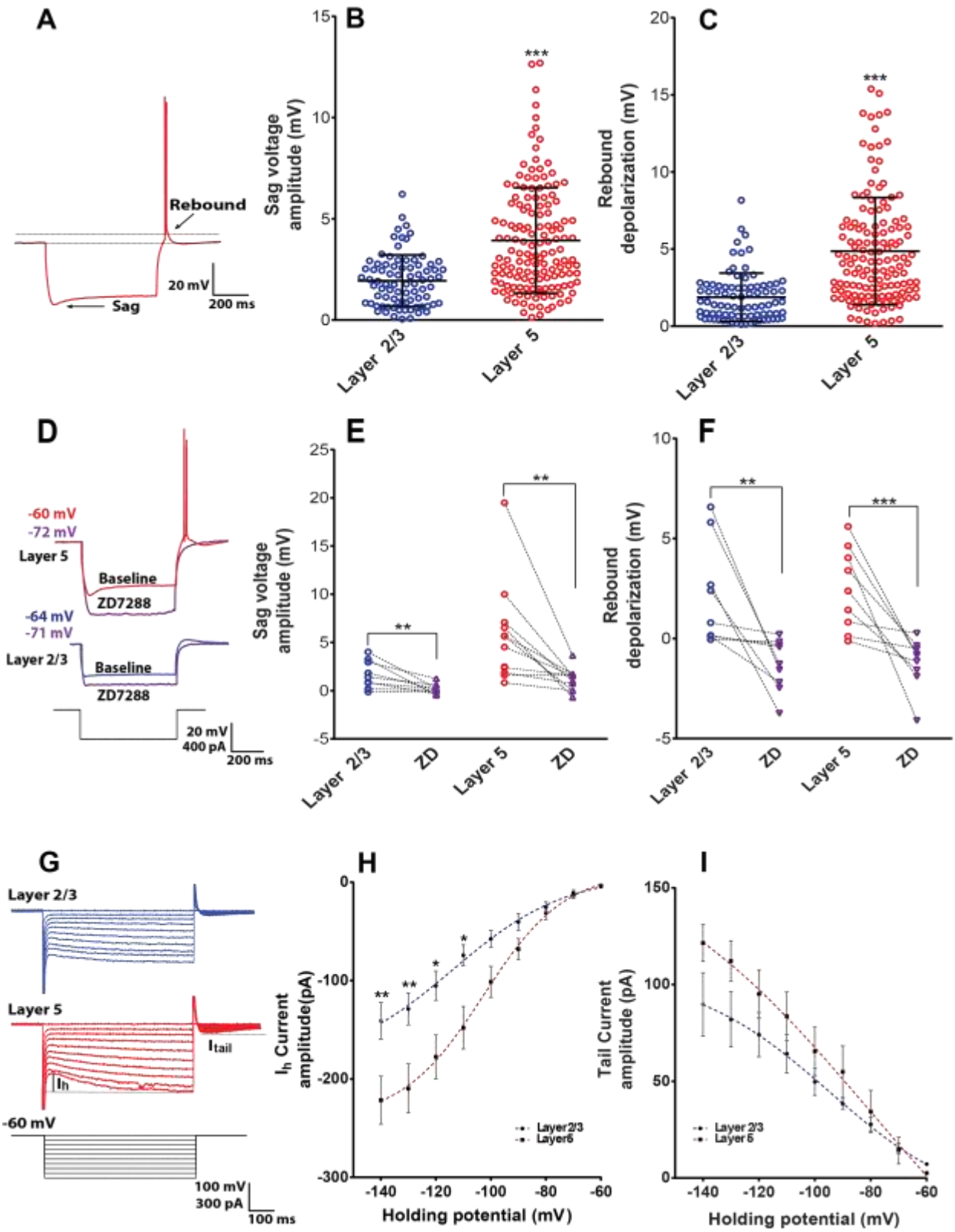

bioRxiv preprint doi: https://doi.org/10.1101/748988; this version posted August 29, 2019. The copyright holder for this preprint (which was not certified by peer review) is the author/funder, who has granted bioRxiv a license to display the preprint in perpetuity. It is made available under aCC-BY-NC-ND 4.0 International license.

Figure 2. I_h related membrane properties are more profound in L5 pyramidal cells compared with L2/3. (A) Sample voltage sweeps of a L2/3 and L5 pyramidal cell during injection of a -400 pA hyperpolarizing current step. Arrows indicate sag voltage and rebound depolarization and post-inhibitory rebound spiking. **(B)** Sag voltage was prominent in L5 pyramidal cells in response to injection of hyperpolarizing current (quantified at a -400 pA step). **(C)** Rebound depolarization associated with I_h also was profound in L5 pyramidal cells compared to L2/3. Error bars in B and C denote SD. **(D)** Example of voltage sweeps before (red, blue) and after (purple) bath application of specific I_h blocker ZD7288 (10 µM). **(E, F)**. Bath application of ZD7288 diminished sag voltage and rebound depolarization in both layers. **(G)** Example voltage-clamp recordings of L2/3 and L5 pyramidal cells. Annotations show calculation of I_h and I_{tail} currents. **(H)** L5 pyramidal cells had significantly larger amplitude I_h currents compared to L2/3 pyramidal cells. **(I)** Quantification of I_h tail current at the end of each holding potential revealed that there was no significant difference between L2/3 and L5. The dashed lines in **I** and **H** indicates the fit to a Boltzmann function. *, **,***, indicate significantly different ($P < 0.001$, $P < 0.05$, $P < 0.001$).

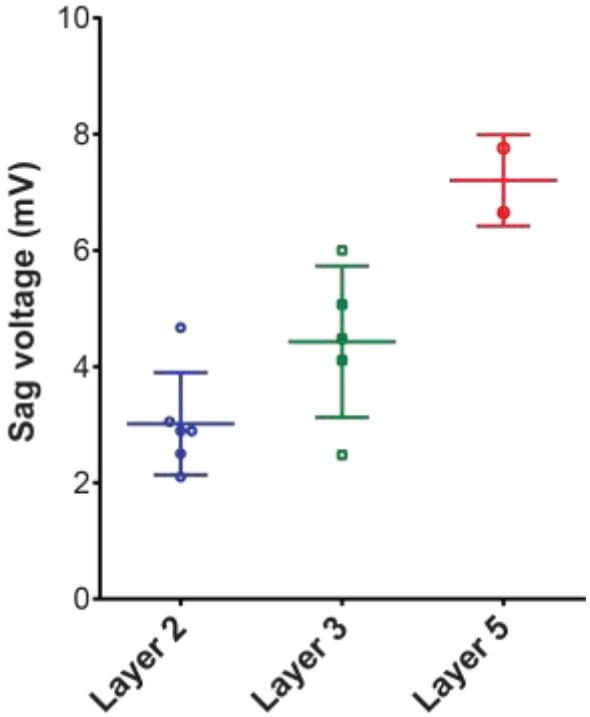

Figure S1: Correlation between sag voltage amplitude and distance from pial surface. We found a positive correlation between sag voltage amplitude and distance from pial surface, replicating this finding as reported previously (Kalmbach, Buchin et al. 2018). These cells were recorded from two patients in a subset of recordings where cortical layer differences between L2 and L3 were explicitly annotated.

bioRxiv preprint doi: https://doi.org/10.1101/748988; this version posted August 29, 2019. The copyright holder for this preprint (which was not certified by peer review) is the author/funder, who has granted bioRxiv a license to display the preprint in perpetuity. It is made available under aCC-BY-NC-ND 4.0 International license.

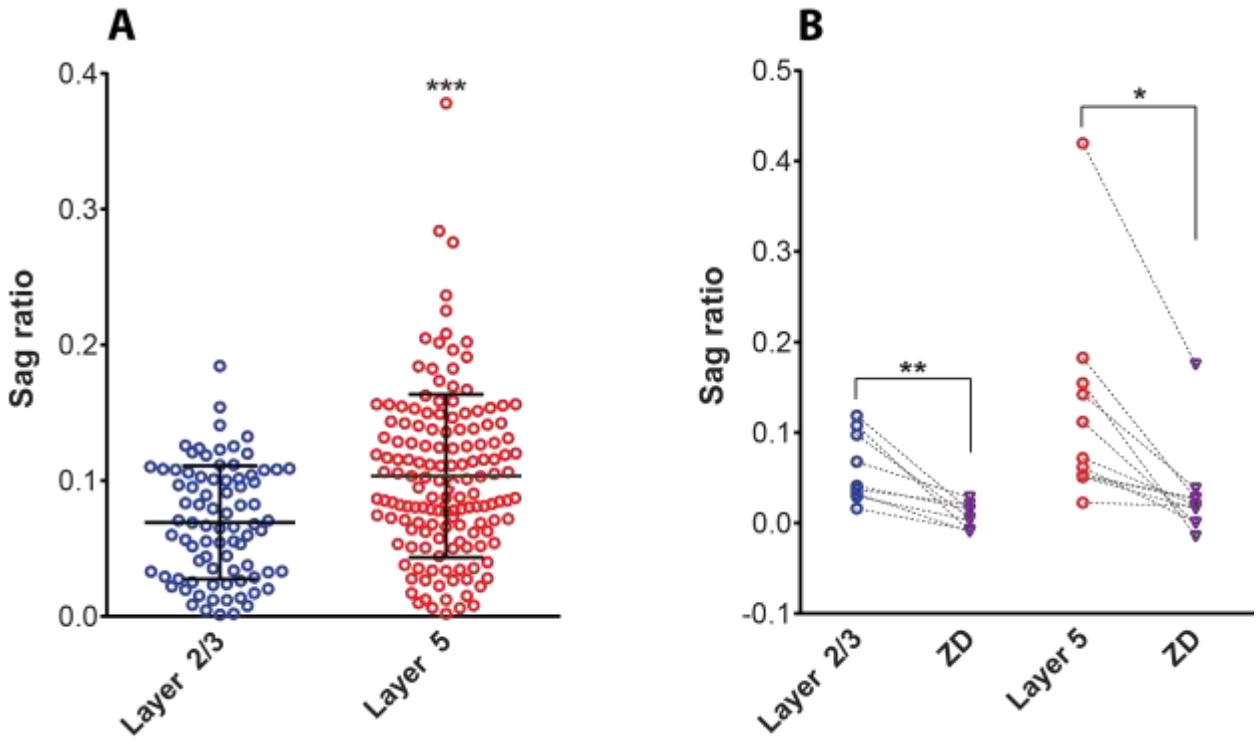

Figure S2: Sag differences between cortical layers are robust to normalizing for input resistance differences using the dimensionless sag ratio mesaure. (A) Same as Fig 2B, but data are plotted using the sag ratio measure. **(B)** Same as Fig 2E, showing bath application of I_h blocker ZD7288 (10 μM) reducing sag ratio in pyramidal cells from both layers.

bioRxiv preprint doi: https://doi.org/10.1101/748988; this version posted August 29, 2019. The copyright holder for this preprint (which was not certified by peer review) is the author/funder, who has granted bioRxiv a license to display the preprint in perpetuity. It is made available under aCC-BY-NC-ND 4.0 International license.

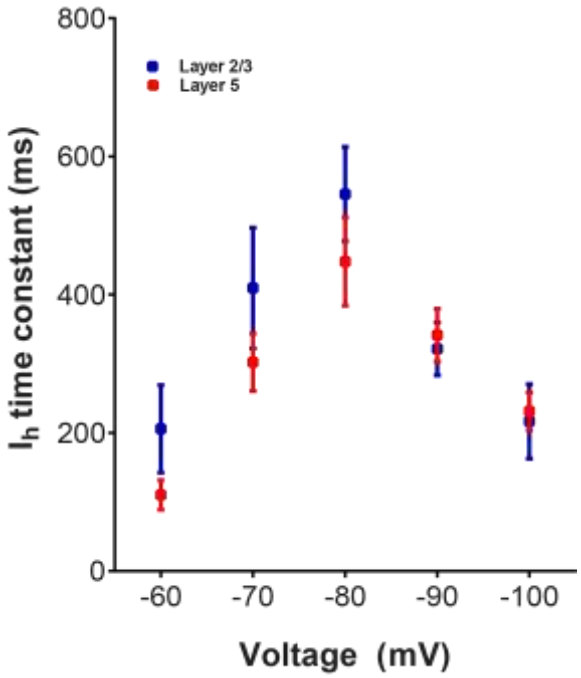

Figure S3: I_h time constant was similar between L2/3 and L5 pyramidal cells. Voltage clamp recordings of I_h current show that I_h time constants are similar between L2/3 and L5 pyramidal cells. These data suggest that the difference between sag voltages in L2/3 and L5 pyramidal cells are not due to differences in the kinetics of HCN channels.

3.3. Suprathreshold active membrane properties of pyramidal cells in layers 2/3 and 5

We next characterized the firing patterns of L2/3 and L5 human pyramidal cells using a series of depolarizing current pulses (50-400 pA, 600ms) with examples shown in Figure 3A and B. The frequency-current relationships (f-I curve) showed greater f-I slopes for L5 relative to L2/3 cells (Figures 3C). L2/3 neurons showed stronger spike frequency adaptation relative to L5 neurons (L2/3: n= 42, 2.65 ± 1.7, L5: n= 63; 1.9 ± 0.93; $p<0.01$, Figures 3D). In addition, the action potential amplitude was significantly larger in L5 compared to L2/3 (L2/3: n= 54, 63 ± 18 mV , L5: n= 128; 74 ± 22 mV $p<0.01$. Moreover, the half-width of the action potential was shorter in L5 pyramidal cells compared to L2/3 pyramidal cells (L2/3: n= 53, 2.1 ± 1.2ms, L5: n= 128; 1.7 ± 1.2ms; $p = 0.07$).

We further characterized the firing patterns of the recorded neurons using previously established criteria (Connors and Gutnick 1990, Chang and Luebke 2007, Zaitsev, Povysheva et al. 2012), with sample traces shown in Figures S4C and D. The majority of pyramidal cells in L2/3 were regular spiking (84%), with the remainder of the cells displaying intrinsically bursting behavior (Figures S4A). The majority of the cells in L5 also were regular spiking (70%), but we found that considerably more (30%) were intrinsically bursting (Figures S4B)

bioRxiv preprint doi: https://doi.org/10.1101/748988; this version posted August 29, 2019. The copyright holder for this preprint (which was not certified by peer review) is the author/funder, who has granted bioRxiv a license to display the preprint in perpetuity. It is made available under aCC-BY-NC-ND 4.0 International license.

bioRxiv preprint doi: https://doi.org/10.1101/748988; this version posted August 29, 2019. The copyright holder for this preprint (which was not certified by peer review) is the author/funder, who has granted bioRxiv a license to display the preprint in perpetuity. It is made available under aCC-BY-NC-ND 4.0 International license.

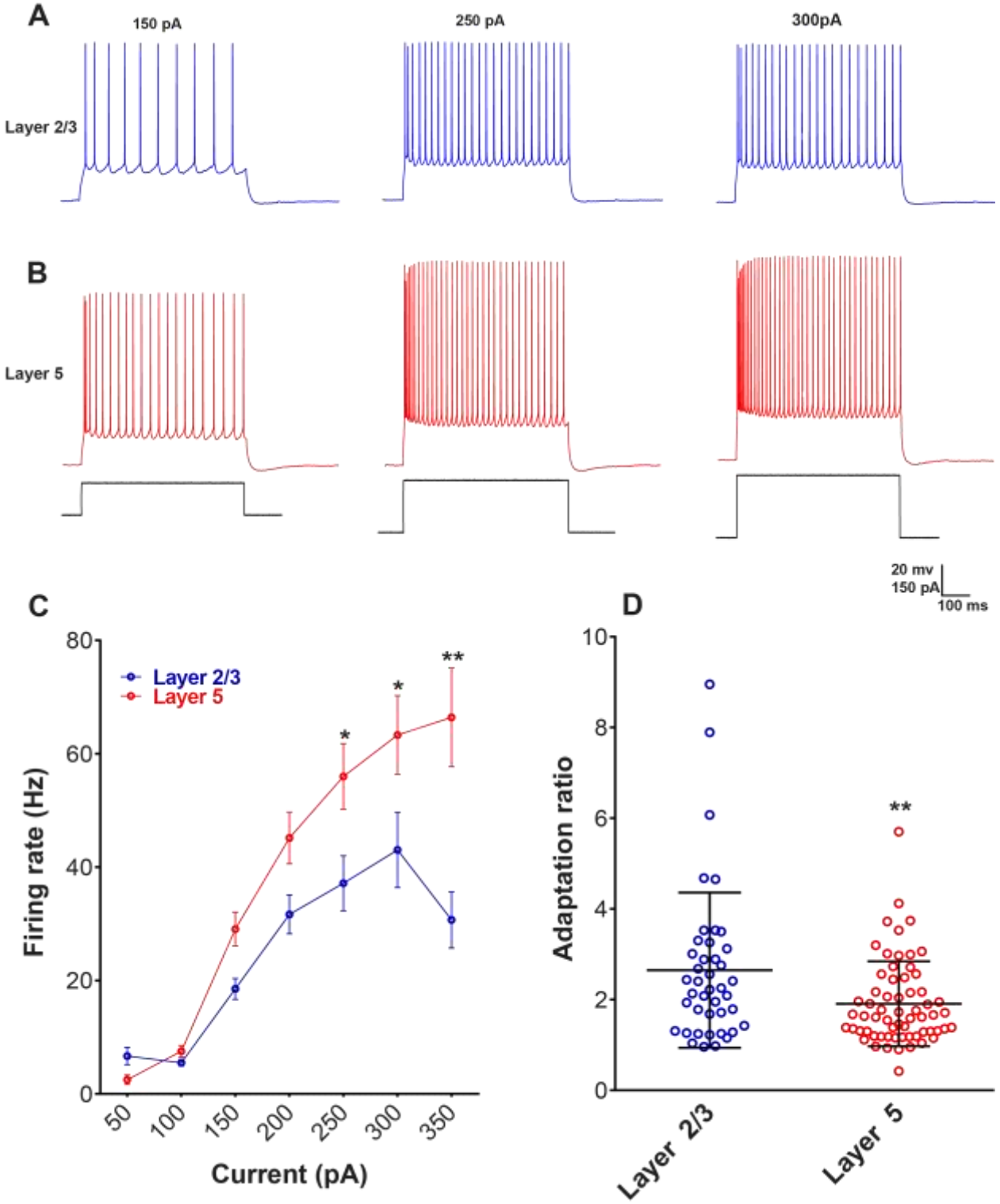

bioRxiv preprint doi: https://doi.org/10.1101/748988; this version posted August 29, 2019. The copyright holder for this preprint (which was not certified by peer review) is the author/funder, who has granted bioRxiv a license to display the preprint in perpetuity. It is made available under aCC-BY-NC-ND 4.0 International license.

Figure 3. L5 pyramidal cells display higher frequency firing rate and less adaptation than L2/3 neurons. (A, B) Example L2/3 and L5 pyramidal cell voltage responses during depolarizing current injections (150 pA, 250 pA and 350 pA, 600 ms). **(C)** L5 in comparison to L2/3 fired at higher frequencies following depolarizing current injections. **(D)** L2/3 and L5 spike frequency adaptation ratio, calculated by dividing the mean of the three last inter-spike intervals to the mean of the three first inter-spike intervals following positive current steps (600 ms duration, 300 pA). L5 pyramidal cells show less spike frequency adaption during injection depolarization in comparison with L2/3. Error bars denote SD. *, ** significantly different ($P < 0.01$, $P < 0.05$).

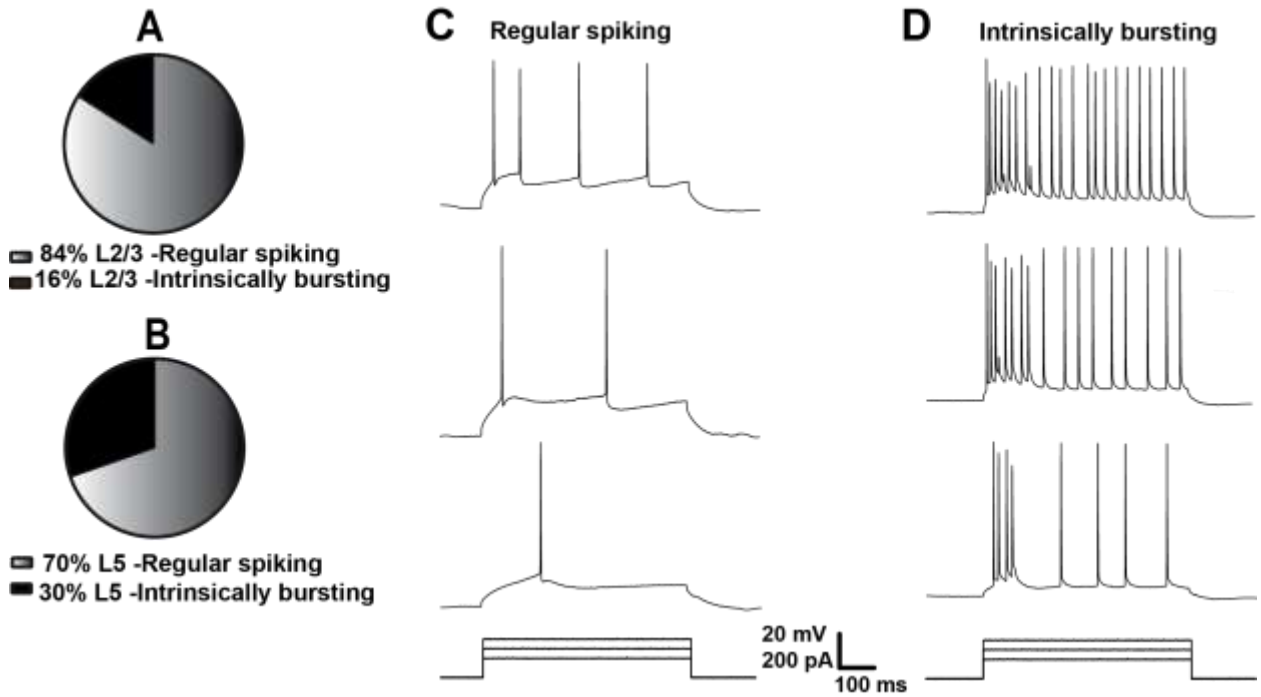

Figure S4: Distribution of different firing patterns across L2/3 and L5 pyramidal cells . (A,B) L2/3 and L5 pyramidal cells tend to have more regular spiking than intrinsically bursting cells. The percentage of intrinsically bursting cells recorded in L5 was higher compared to L2/3. (C, D) Example voltage traces of regular spiking and intrinsically bursting cells during depolarizing current injections.

3.4. L5 pyramidal track low and high frequency stimuli better than L2/3 cells

The differences in L2/3 and L5 pyramidal cell active and passive membrane properties suggest that these neurons would have different responses to similar types of inputs. Resonance is a common approach to characterizing the frequency preferences of neurons and represents the net result of the interaction between passive and active properties (Hutcheon and Yarom 2000). I_h is an active current shown to contribute to low pass filtering properties of pyramidal cells due to its slow activation and deactivation (Hu, Vervaeke et al. 2002). Indeed, human L3 pyramidal cells, which display a larger sag voltage than superficial L2, also exhibit low frequency membrane resonance (Kalmbach, Buchin et al. 2018). The findings by

bioRxiv preprint doi: https://doi.org/10.1101/748988; this version posted August 29, 2019. The copyright holder for this preprint (which was not certified by peer review) is the author/funder, who has granted bioRxiv a license to display the preprint in perpetuity. It is made available under aCC-BY-NC-ND 4.0 International license.

Kalmbach et al. in human neurons are consistent with initial studies in rodent cortex that describe the correlation between a large sag voltage and low frequency resonance (Hutcheon, Miura et al. 1996).

Given the larger sag voltage amplitudes in L5 relative to L2/3 pyramidal cells, we reasoned that that L5 pyramidal cells would also display low frequency resonance. To explore this, we examined subthreshold resonance of L2/3 and L5 cells using a 20s-long ZAP current stimulus (Puil, Gimbarzevsky et al. 1986) with example traces shown in Figure 4A. At the resting membrane potential, we surprisingly we found that neither L2/3 nor L5 pyramidal cells display a peak in the impedance profiles (Figure 4C).

To further compare the frequency response characteristics of L2/3 and L5 pyramidal cells, we modified our ZAP protocol to deliver current at suprathreshold amplitudes, with example traces shown in Figure 4B. We found that L5 cells spike with greater fidelity to higher frequency stimuli (12-18 Hz) relative to L2/3. We did not observe a difference in frequency tracking at other frequency ranges (Figure 4D), including frequencies at delta or theta (1-12 Hz), consistent with their subthreshold impedance profiles. We found qualitatively similar results when repeating the ZAP current injection while holding cells near -80 mV (data not shown).

bioRxiv preprint doi: https://doi.org/10.1101/748988; this version posted August 29, 2019. The copyright holder for this preprint (which was not certified by peer review) is the author/funder, who has granted bioRxiv a license to display the preprint in perpetuity. It is made available under aCC-BY-NC-ND 4.0 International license.

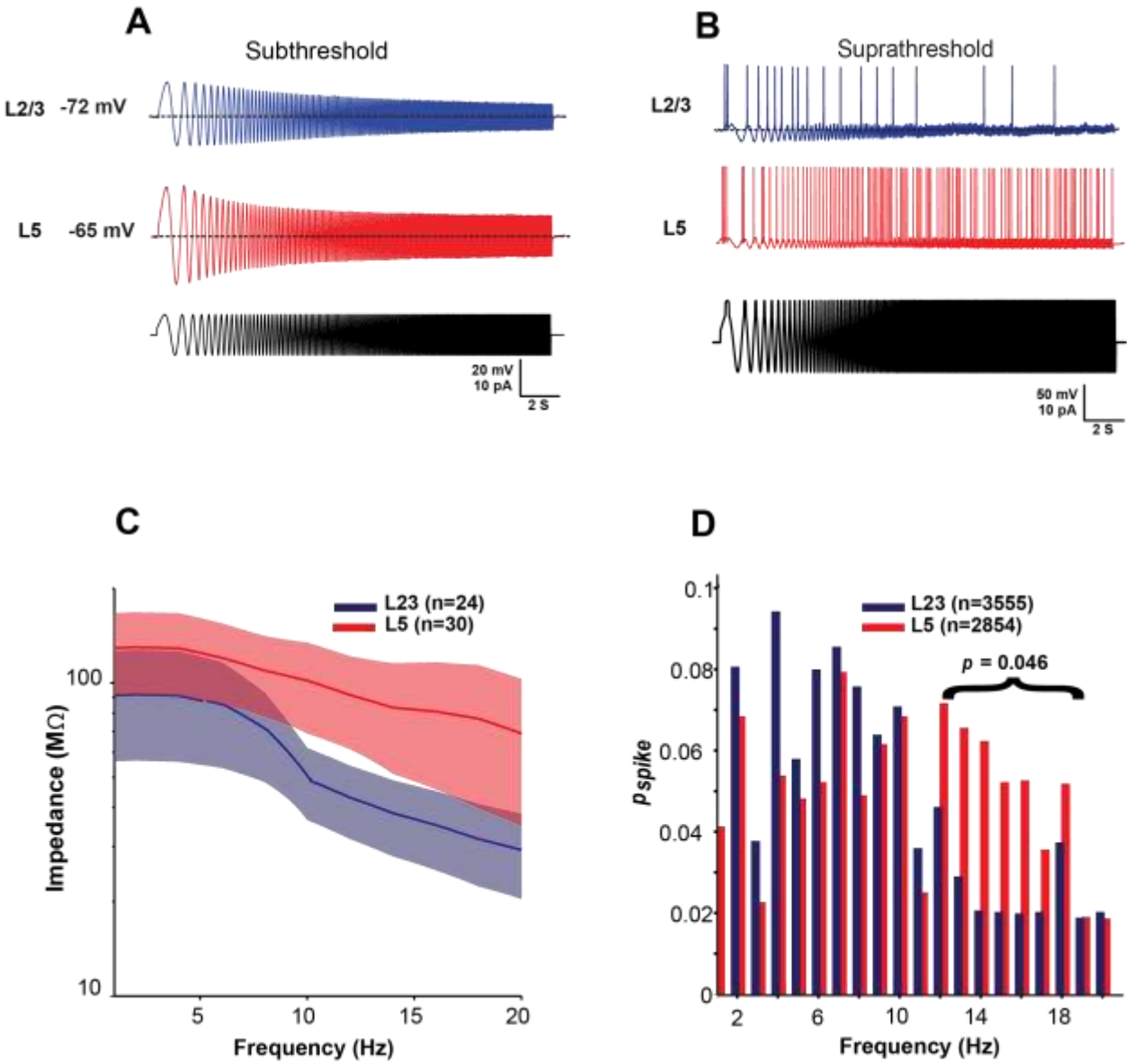

Figure 4. L2/3 and L5 pyramidal cells do not intrinsically resonate, acting as low pass filters to sub- and suprathreshold inputs. (A, B) Example of voltage responses following injection of subthreshold (A) and suprathreshold (B) ZAP current delivered at RMP in a L5 and L2/3 pyramidal cell. **(C)** The impedance frequency profiles of L2/3 and L5 pyramidal cells reveal that both cell types act as low pass filters. We did not see a characteristic peak at theta frequencies in either cell type. **(D)** Spike response probability in response to suprathreshold current injection show that both layers track theta frequencies with high fidelity. The distributions were not significantly different (KSp = 0.53). Above 12Hz spike probabilities differed significantly between L2/3 and L5.

bioRxiv preprint doi: https://doi.org/10.1101/748988; this version posted August 29, 2019. The copyright holder for this preprint (which was not certified by peer review) is the author/funder, who has granted bioRxiv a license to display the preprint in perpetuity. It is made available under aCC-BY-NC-ND 4.0 International license.

To further characterize frequency dependent suprathreshold spiking properties of L2/3 and L5 pyramidal cells, in a subset of cells (n=8 cells each for L5 and L2/3) from an additional set of patients (n=5) we adapted our slice preparation and recording protocols (Ting, Daigle et al. 2014) to study the frequency preference for spiking (see Methods). We stimulated cells with multiple trials of a frozen filtered noise current injection stimulus. We used this stimulus to compute the frequency dependent gain [*G(f)*] and the mean phase shift of the spike response (Figure 5A) (Higgs and Spain 2009). The frequency dependent gain, *G(f)*, quantifies the phase preference of neuronal spiking as function of frequency (Yu and Lewis 1989); intuitively, neurons with a high gain at a specific frequency are more likely to fire in phase with a sine-wave at that frequency than at other frequencies.

We found both that L2/3 and L5 cells displayed peaks in *G(f)* within the delta and theta frequency ranges (Figure 5B). Both peaks were more pronounced in L5 pyramidal cells compared to L2/3 ($p<0.05$). Additionally, above 10Hz, we found that L5 pyramidal cells displayed greater frequency dependent gain than L2/3 cells, consistent with the suprathreshold ZAP results. The greater excitability and fidelity of L5 neurons was also evident in their phase curves and spike triggered averages (STAs) (Figure 5C, D). L2/3 neurons demonstrated a greater lag in firing than L5 neurons, and their STA were of larger amplitude with steeper slopes, suggesting that L2/3 neurons require larger inputs to trigger spikes, and when they do spike they will lag behind L5 pyramidal cells if inputs are coincident.

bioRxiv preprint doi: https://doi.org/10.1101/748988; this version posted August 29, 2019. The copyright holder for this preprint (which was not certified by peer review) is the author/funder, who has granted bioRxiv a license to display the preprint in perpetuity. It is made available under aCC-BY-NC-ND 4.0 International license.

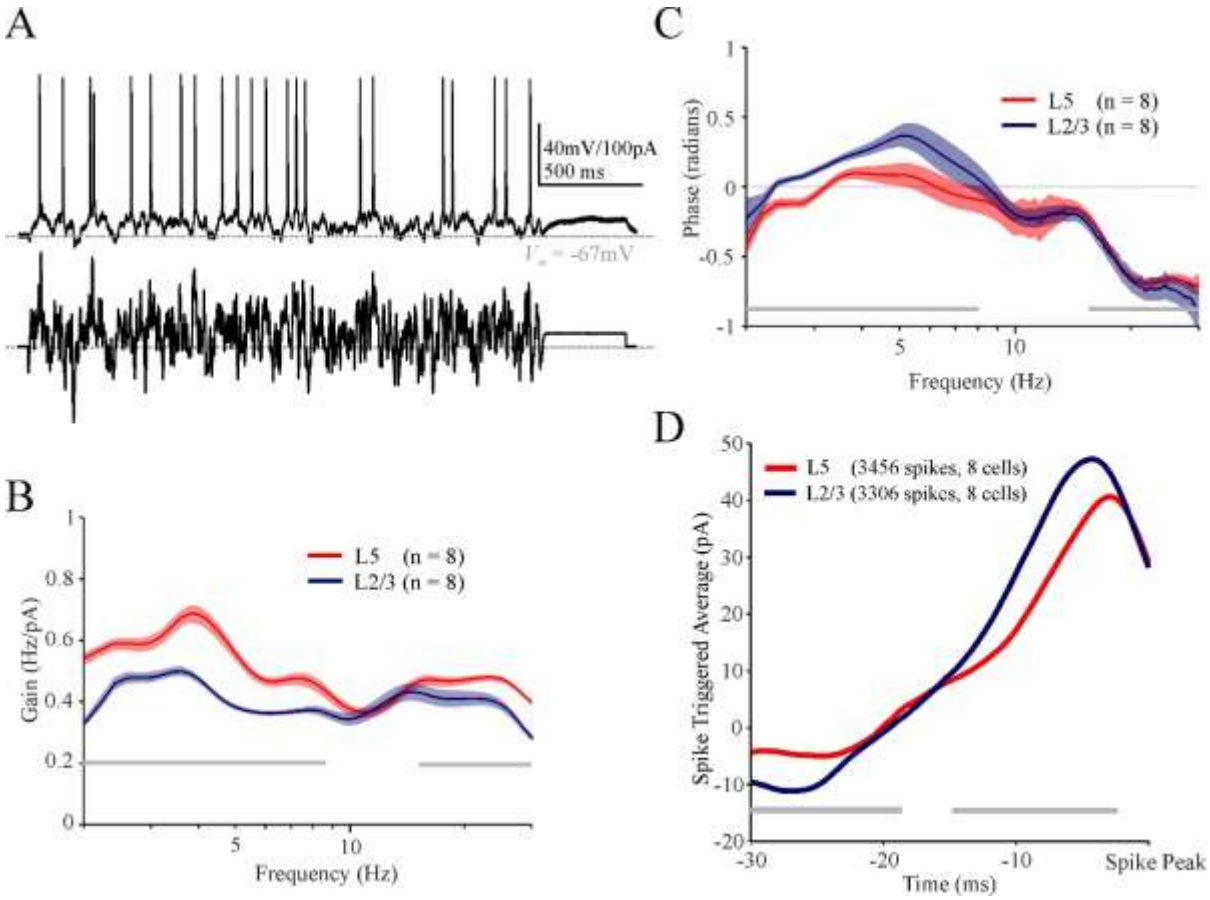

Figure 5: Human L5 neurons display greater gain at delta and theta frequencies than L2/3 pyramidal neurons. (A) Example of V_m response to 2.5s of frozen filtered noise current injection stimulus for a L5 pyramidal cell. **(B)** Frequency dependent gain profile of L2/3 and L5 pyramidal cells over a wide range of frequencies. Frequency dependent gain, *G(f)*, was calculated with frequency-dependent windowing (see Materials and Methods). Both layers show two peaks around 2.5-10 Hz, and 12-16 Hz which are more pronounced in L5 pyramidal cells compared to L2/3. Gray horizontal bars represent significant differences between groups. **(C)** Phase shift of spiking relative to input stimulus. L2/3 pyramidal cells show positive phase in their mean phase shift profile which represents a lag in L2/3 pyramidal cells compared to L5 pyramidal cells. **(D)** Mean spike triggered average (STAs) for L5 and L2/3 cells. Difference in STAs indicate L5 cells require less current and instantaneous rate of current increase to initiate a spike (greater excitability).

3.5. Pyramidal cell sag correlates with patient age

Lastly, we investigated if some of the cell-to-cell variability in sag and other intrinsic features could be in part explained by patient-level demographic features, such as age at time of surgery. To address this question, we cross-referenced our recordings with basic demographic information from patient medical records where available, yielding a total of 159 cells from 36 patients. We further utilized a dataset of 272 pyramidal cells sampled from layers 2, 3, and 5 from an additional cohort of 39 human surgical patients characterized by the Allen Institute for Brain Sciences (http://celltypes.brain-map.org/). We note that while

bioRxiv preprint doi: https://doi.org/10.1101/748988; this version posted August 29, 2019. The copyright holder for this preprint (which was not certified by peer review) is the author/funder, who has granted bioRxiv a license to display the preprint in perpetuity. It is made available under aCC-BY-NC-ND 4.0 International license.

the overall experimental design of the Allen Institute's dataset is similar to ours, there are some key methodological differences, such as the composition of solutions used for slice preparation and recording (see Methods). In addition, because of differences in the amplitudes of hyperpolarizing current steps used to assess sag, we chose to cross-compare these datasets using the dimensionless sag ratio measure, defined as the ratio between the sag amplitude and the hyperpolarization-evoked peak voltage deflection from the resting potential. We note that sag ratio is positively correlated with sag amplitudes (Figure S5, r = 0.68).

In the L5 pyramidal cells sampled in our dataset (the Krembil Institute cohort), we found that cells recorded from older patients tended to have larger sag ratios than those from younger patients (Figure 6A, r = 0.30, p = 0.015 based on a mixed-effects statistical model with subject ID as a random effect, see Methods). Importantly, when we investigated analogous L5 pyramidal cells from the Allen Institute cohort, we found a consistent relationship between patient age and sag ratios that was also statistically significant (Figure 6B, r = 0.30, p = 0.020). Assessing this relationship in L2/3 pyramidal cells, we found a similar overall relationship in data from the Krembil Institute cohort (Figure 6C, r = 0.38, p = 0.024). While we found a relationship in the same direction in the Allen Institute cohort for L2/3 cells, we note that the relationship was not statistically significant (Figure 6D, r = 0.11, p = 0.30), possibly due to differences in the relative compositions of L2 versus L3 pyramidal cells sampled in each cohort. In addition, we were able to use the Allen Institute cohort dataset to validate our earlier finding that L5 pyramidal cells have larger sag ratios than superficial layer pyramidal cells (p, Wilcox test = 0.00055).

bioRxiv preprint doi: https://doi.org/10.1101/748988; this version posted August 29, 2019. The copyright holder for this preprint (which was not certified by peer review) is the author/funder, who has granted bioRxiv a license to display the preprint in perpetuity. It is made available under aCC-BY-NC-ND 4.0 International license.

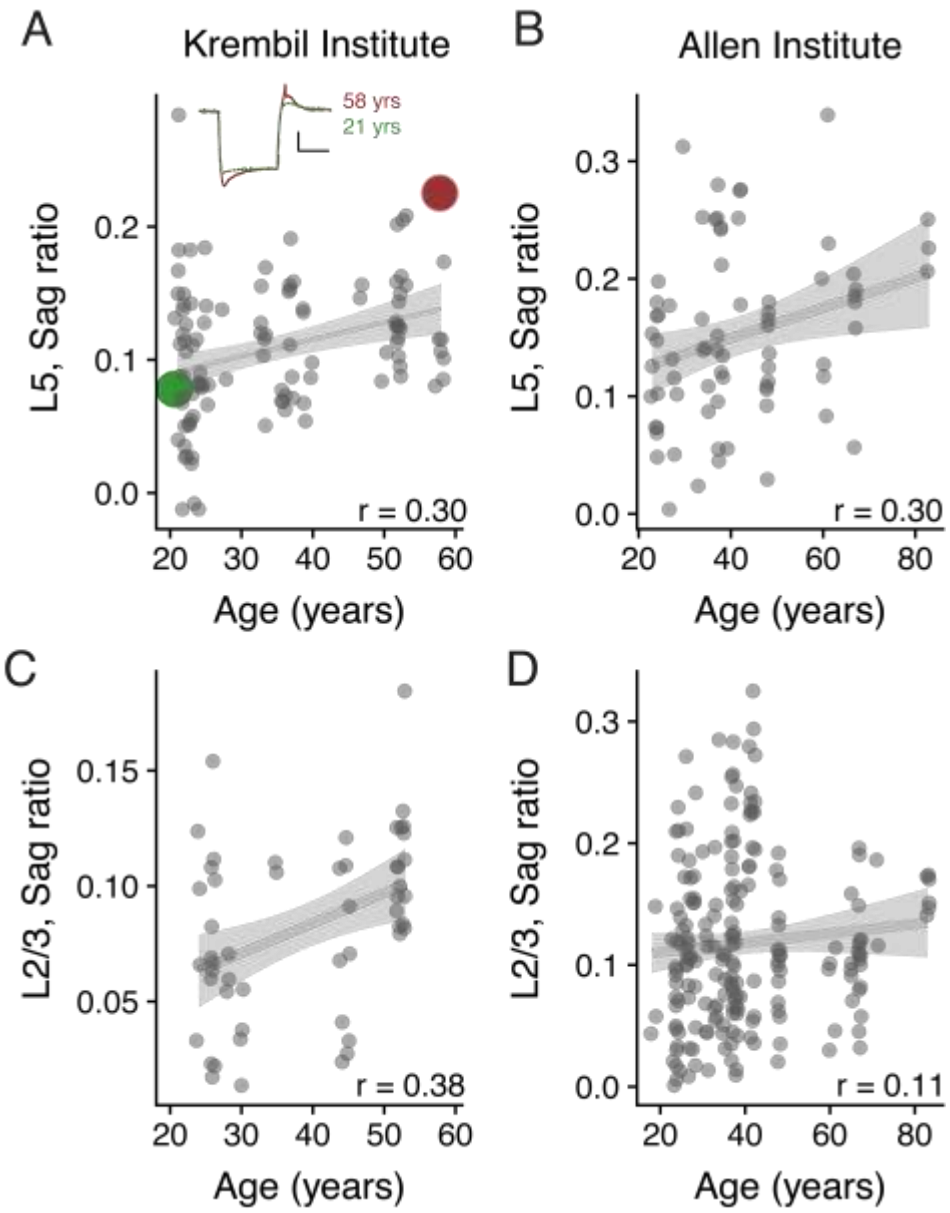

Figure 6: Correlation between pyramidal cell sag ratios and patient age. (A) L5 pyramidal cell sag ratio values as a function of patient age for cells sampled from the Krembil Institute cohort. Each grey dot reflects one cell and multiple cells are typically sampled per patient. Inset shows example voltage trace data for two representative cells. Grey line indicates linear fit. Inset correlation values based on a linear mixed effects model. **(B)** Same as A, but for data from the Allen cohort. **(C-D)** Same as A and B, but for L2/3 pyramidal cells sampled from the Krembil Institute cohort (C) or the Allen Institute cohort (D).

bioRxiv preprint doi: https://doi.org/10.1101/748988; this version posted August 29, 2019. The copyright holder for this preprint (which was not certified by peer review) is the author/funder, who has granted bioRxiv a license to display the preprint in perpetuity. It is made available under aCC-BY-NC-ND 4.0 International license.

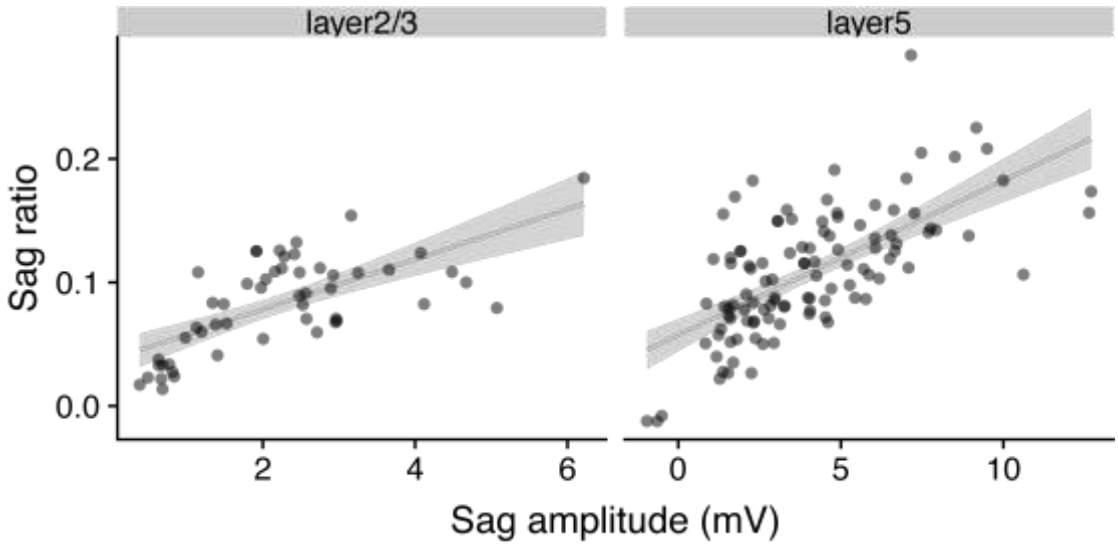

Figure S5: Correlation between sag voltage and sag ratio in data from the Kremibl Institute cohort.

4. Discussion

4.1. Distinct electrophysiological properties of L2/3 and L5 pyramidal neurons in human temporal cortex

Guided by our previous work implicating deep layer human pyramidal neurons in the genesis and propagation of theta rhythms, we sought to characterize the electrophysiological differences between deep and superficial human pyramidal cells. We found that L2/3 pyramidal neurons demonstrated overall less excitability relative to L5 pyramidal cells, with L2/3 pyramidal cells exhibiting broader action potentials, lower firing rates, enhanced spike frequency accommodation, and steeper and larger amplitude spike triggered averages. These basic findings are consistent with a number of previous studies in rodents suggesting that L5 cells are more excitable than L2/3 cells (Petersen, Hahn et al. 2003, Crochet and Petersen 2006, Poulet and Petersen 2008, Crochet, Poulet et al. 2011).

We found that L5 pyramidal cells had significantly greater I_h relative to L2/3 cells as evidenced by a larger sag voltage in current clamp mode. Furthermore, I_h appeared to be one of the major contributors to the prominent post-inhibitory depolarization and rebound spiking in human L5 cells since ZD7288 significantly reduced both. To further dissect the I_h current in L5 and L2/3 cells we used pharmacology and

bioRxiv preprint doi: https://doi.org/10.1101/748988; this version posted August 29, 2019. The copyright holder for this preprint (which was not certified by peer review) is the author/funder, who has granted bioRxiv a license to display the preprint in perpetuity. It is made available under aCC-BY-NC-ND 4.0 International license.

voltage clamp analyses to reveal that the amplitude but not the kinetics of I_h differ between the layers. This finding suggests that the differences in currents expressed in deep versus superficial pyramidal cells are likely a result of a greater density of HCN channels and are not due to differences in subunit composition between layers. We note that at present it is unclear whether this difference in channel density is due to increased insertion of channels at the soma or differential insertion along the dendrites (Robinson and Siegelbaum 2003).

4.2. Relationships between I_h and cortical rhythmogenesis in human pyramidal cells

Given our findings of greater I_h currents in L5 cells, we were initially surprised that they did not demonstrate subthreshold resonance. For example, a previous report by Kalmbach et al, suggested that in human I_h contributes to subthreshold resonance at 4 Hz in deep L3 pyramidal neurons (Kalmbach, Buchin et al. 2018). In addition, previous work in rodents has shown that L5 pyramidal cells are associated with the genesis of subthreshold frequency resonance, especially in the slow <1 Hz and delta 1-4 Hz frequency bands (Silva, Amitai et al. 1991, Ulrich 2002, Dembrow, Chitwood et al. 2010, Schmidt, Dorsett et al. 2016). It has been proposed that this band pass filtering is mediated by interactions between I_h current (Ulrich 2002), persistent Na^+ current (I_{Nap}), I_{IR} (instantaneously activating, inwardly rectifying K^+ current) (Dembrow, Chitwood et al. 2010), I_M current and passive properties of L5 pyramidal cells (Schmidt, Dorsett et al. 2016). However, previous investigations of subthreshold theta resonance have shown that I_h alone is not sufficient to account for the high pass filtering that gives rise to a resonant peak; in fact, it is likely a more complex interaction of the presence of I_h, along with the kinetics of this channel, the neuron's morphology, and its passive properties, that dictates whether a cell will demonstrate a low frequency resonant peak.

In this context, hippocampal oriens-lacunosum molecular (OLM) interneurons, for example, exhibit a large characteristic sag, indicative of the presence of I_h, without displaying subthreshold theta resonance (Zemankovics, Káli et al. 2010). When comparing OLM cells to CA1 pyramidal cells as well as oriens-radiatum (OR) interneurons that have I_h and theta resonance, Zemankovics et. al. identified minimal difference in the I_h conductance between the three neuron types. Instead, a significant difference in the voltage dependence of the h-channel kinetics was identified between the two interneuron types and the pyramidal cells, but not between the OLM and OR interneurons, indicating that these kinetics might account for some, but not all, of the tendency of these cells to resonate. Zemankovics et. al. further suggest that differences in passive properties between the OLM and OR cells underlie the different resonance characteristics in these interneurons. The work of Hu et. al identified multiple mechanisms by which resonance can occur, including one mediated by the m-current (Hu, Vervaeke et al. 2002). Additionally, in inferior olivary neurons it is the low threshold calcium current that underlies these neurons' low frequency resonance (Lampl and Yarom 1997), implying I_h is neither necessary nor sufficient in the generation of low frequency resonance. Taken together, these results paint a more complicated picture of the relationship between the presence of I_h and the capacity for a neuron to exhibit subthreshold resonance, a situation wanting for computational modeling and in silico explorations to help fully describe this aspect of human L5 physiology (Einevoll, Destexhe et al. 2019).

Recently a putative 'dynamic circuit motif' (DCM) (Womelsdorf, Valiante et al. 2014) has been proposed as a mechanism for explaining interlaminar nested delta-theta oscillations observed in rodents. This DCM posits L5 IB neurons as a central actor in generating deep layer activity that drives superficial theta oscillations (Carracedo, Kjeldsen et al. 2013). Although, the electrophysiological signature and experimental conditions studied in Carracedo et al were different that our studies in human cortical slices, it is instructive to relate our findings to what was observed in rat neocortex. Carracedo et al., demonstrated that delta oscillations likely occur due to tonic drive to the dendrites of IB neurons in superficial layers. This tonic drive causes the IB neurons to discharge bursts at delta frequencies. IB cells are unique in that in

bioRxiv preprint doi: https://doi.org/10.1101/748988; this version posted August 29, 2019. The copyright holder for this preprint (which was not certified by peer review) is the author/funder, who has granted bioRxiv a license to display the preprint in perpetuity. It is made available under aCC-BY-NC-ND 4.0 International license.

addition to their subcortical targets, they primarily synapse locally within deep layers on L5 RS neurons, unlike L5 RS neurons that project axons both locally and to L2/3 (Larsen, Wickersham et al. 2008). The RS cells are thus driven by periodic barrages at delta frequencies, and discharge doublets with each IB burst and thus generating theta frequency output that is transmitted to superficial layers. The sinks generated in the superficial layers thus occur at theta frequency, driving local excitability in L2/3 with the resultant increase in excitatory drive to L5 IB dendrites and the cycle begins.

Our data demonstrates that human L5 has a greater percentage of IB pyramidal cells (30%) in comparison to L2/3, although the proportion of IB relative to RS cells is necessary but not sufficient for generating nested theta rhythms by the DCM mechanism. In those cells in which we computed frequency dependent gain, *G(f)*, it appears that human L5 neurons synchronize well to both delta and theta frequencies. Assuming that we primarily recorded from RS neurons, one possible explanation for the shape of the *G(f)* curve for L5 neurons is that they are tuned to receive delta frequency inputs from IB cells, while at the same time amplifying locally generated theta activity. It is important to note that the *G(f)* we observed for human L5 neurons (and L2/3 neurons) was different from rodent L2/3 pyramidal cells, demonstrating a single peak at theta (Higgs and Spain 2009). The increase in gain in rodent L2/3 neurons was demonstrated to represent the time between action potential bursts, governed in part by the medium after-hyperpolarization (mAHP) time constant. Such a mechanism might be at play in human L5 neurons, however this would require further investigation.

An obvious difference between our previous human slice work (Florez, McGinn et al. 2013) and that of Carracedo et al. is that we observed robust deep layer theta (although theta was still more prominent in the superficial layers). One possible explanation is that the experimental conditions were dramatically different. Alternatively it has been shown that in human cortical tissue, at least in L2/3, that single action potentials generate long lasting reverberant activity that lasts an order of magnitude longer than in the rodent brain (Molnár, Oláh et al. 2008). It is thus possible that this reverberant activity results in greater gain in local L5 cortical circuits that amplifies theta activity generated by IB driven RS cells theta spiking (Carracedo, Kjeldsen et al. 2013), through both synaptic activation and increased theta frequency *G(f)*. Future experiments are needed to further explore if human cortical circuitry is arranged like that of the rodent - specifically as it relates to inter- and intralaminar connectivity.

4.3. Correlating between-patient differences in electrophysiological features with patient demographics

Leveraging the large sample of patients in our study, we asked if there were correlations between the basic demographic features of these individuals and the electrophysiological characteristics of their neurons. We found that pyramidal cells from recorded older patients tended to show greater amounts of sag relative to pyramidal cells recorded in younger patients, with this correlation appearing largely driven by age-related differences in deep pyramidal cells. By replicating this finding using publicly-accessible data collected by the Allen Institute from a second cohort of human patients, we were able to gain additional confidence in the generalizability of this relationship. There are a number of potential implications for this relationship that necessitate further study and it is exciting to speculate that this electrophysiological change might further be associated with age-related downstream changes at the circuit and cognitive levels.

4.4. Limitations and caveats

An important caveat when interpreting these findings is that these data are exclusively collected from neurosurgical patients undergoing surgery for drug-resistant epilepsy or for resection of brain tumors. We note that we have been careful to only perform recordings from unaffected neocortical tissue distal from the epilepsy focus or tumor site. Nevertheless, it is unclear how these diseases (or their

bioRxiv preprint doi: https://doi.org/10.1101/748988; this version posted August 29, 2019. The copyright holder for this preprint (which was not certified by peer review) is the author/funder, who has granted bioRxiv a license to display the preprint in perpetuity. It is made available under aCC-BY-NC-ND 4.0 International license.

pharmacological treatment regimes) might contribute to compensatory changes at the level of cortical neuron physiology. However, by comparing our findings to the previous rich literature in rodents and to analogous human neuronal datasets collected by other groups, we are more confident that the results presented here likely generalize to control human subjects.

4.5. Future implications of this work

This report reflects one of the largest studies of the electrophysiological diversity of human neocortical pyramidal neurons to date. In particular, it contributes to our growing understanding of human L5 pyramidal neurons (Beaulieu-Laroche, Toloza et al. 2018) and helps put the unique characteristics of these cells into context with better understood superficial layer pyramidal cells.

Moving forward, it will be essential to reconcile these electrophysiological and morphological data with the emerging consensus of neocortical cell type diversity based on single-cell transcriptomics (Habib, Avraham-Davidi et al. 2017, Hodge, Bakken et al. 2018, Kalmbach, Buchin et al. 2018) and how these features contribute to the unique emergent properties of human cortical circuits. Furthermore, little is known about the connectivity within human cortical circuits. Is human inter- and intra laminar connectivity similar to rodents, and how do cellular properties contribute to the signatures we observe in meso- and macroscopic recordings? Answers to these questions will require multi-scale inquires of human cortical micro-circuits and in-silico experiments to understand what are the divergent properties of human circuits – the tools for such inquiries are only now becoming available.

Acknowledgements

We are immensely grateful to our neurosurgical patients and their families for consenting the use of human brain tissue samples for research. We also thank Dr. Gelareh Zadeh and Dr. Mark Bernstein for assistance obtaining brain tissue samples. We thank Etay Hay and Jasmine Bell for critical comments on the manuscript. SJT acknowledges generous start-up support from the CAMH Foundation and the Krembil Foundations.

bioRxiv preprint doi: https://doi.org/10.1101/748988; this version posted August 29, 2019. The copyright holder for this preprint (which was not certified by peer review) is the author/funder, who has granted bioRxiv a license to display the preprint in perpetuity. It is made available under aCC-BY-NC-ND 4.0 International license.

References

Anderson, D. and K. Burnham (2004). "Model selection and multi-model inference." Second. NY: Springer-Verlag **63**.

Bates, D., M. Mächler, B. Bolker and S. Walker (2014). "Fitting linear mixed-effects models using lme4." arXiv preprint arXiv:1406.5823.

Beaulieu-Laroche, L., E. H. Toloza, M.-S. van der Goes, M. Lafourcade, D. Barnagian, Z. M. Williams, E. N. Eskandar, M. P. Frosch, S. S. Cash and M. T. Harnett (2018). "Enhanced dendritic compartmentalization in human cortical neurons." Cell **175**(3): 643-651. e614.

Benjamini, Y. and Y. Hochberg (1995). "Controlling the false discovery rate: a practical and powerful approach to multiple testing." Journal of the royal statistical society. Series B (Methodological): 289-300.

Boldog, E., T. E. Bakken, R. D. Hodge, M. Novotny, B. D. Aevermann, J. Baka, S. Bordé, J. L. Close, F. Diez-Fuertes and S.-L. Ding (2018). "Transcriptomic and morphophysiological evidence for a specialized human cortical GABAergic cell type." Nature neuroscience **21**(9): 1185.

Carracedo, L. M., H. Kjeldsen, L. Cunnington, A. Jenkins, I. Schofield, M. O. Cunningham, C. H. Davies, R. D. Traub and M. A. Whittington (2013). "A neocortical delta rhythm facilitates reciprocal interlaminar interactions via nested theta rhythms." Journal of Neuroscience **33**(26): 10750-10761.

Chang, Y.-M. and J. I. Luebke (2007). "Electrophysiological diversity of layer 5 pyramidal cells in the prefrontal cortex of the rhesus monkey: in vitro slice studies." Journal of neurophysiology **98**(5): 2622-2632.

Connors, B. W. and M. J. Gutnick (1990). "Intrinsic firing patterns of diverse neocortical neurons." Trends in neurosciences **13**(3): 99-104.

Crochet, S. and C. C. Petersen (2006). "Correlating whisker behavior with membrane potential in barrel cortex of awake mice." Nature neuroscience **9**(5): 608-610.

Crochet, S., J. F. Poulet, Y. Kremer and C. C. Petersen (2011). "Synaptic mechanisms underlying sparse coding of active touch." Neuron **69**(6): 1160-1175.

Das, A. and R. Narayanan (2017). "Theta-frequency selectivity in the somatic spike-triggered average of rat hippocampal pyramidal neurons is dependent on HCN channels." Journal of neurophysiology **118**(4): 2251-2266.

Dembrow, N. C., R. A. Chitwood and D. Johnston (2010). "Projection-specific neuromodulation of medial prefrontal cortex neurons." Journal of Neuroscience **30**(50): 16922-16937.

Einevoll, G. T., A. Destexhe, M. Diesmann, S. Grün, V. Jirsa, M. de Kamps, M. Migliore, T. V. Ness, H. E. Plesser and F. Schürmann (2019). "The scientific case for brain simulations." Neuron **102**(4): 735-744.

Eyal, G., M. B. Verhoog, G. Testa-Silva, Y. Deitcher, J. C. Lodder, R. Benavides-Piccione, J. Morales, J. DeFelipe, C. P. de Kock and H. D. Mansvelder (2016). "Unique membrane properties and enhanced signal processing in human neocortical neurons." Elife **5**: e16553.

Florez, C., R. McGinn, V. Lukankin, I. Marwa, S. Sugumar, J. Dian, L.-N. Hazrati, P. Carlen, L. Zhang and T. Valiante (2013). "In vitro recordings of human neocortical oscillations." Cerebral Cortex **25**(3): 578-597.

Galán, R. F., G. B. Ermentrout and N. N. Urban (2008). "Optimal time scale for spike-time reliability: theory, simulations, and experiments." Journal of neurophysiology **99**(1): 277-283.

Gastrein, P., C. Gasselin, R. H. Cudmore, A. Bialowas, E. Carlier, L. Fronzaroli-Molinieres, N. Ankri and D. Debanne (2011). "The role of hyperpolarization-activated cationic current in spike-time precision and intrinsic resonance in cortical neurons in vitro." The Journal of physiology **589**(15): 3753-3773.

Goriounova, N. A., D. B. Heyer, R. Wilbers, M. B. Verhoog, M. Giugliano, C. Verbist, J. Obermayer, A. Kerkhofs, H. Smeding and M. Verberne (2018). "Large and fast human pyramidal neurons associate with intelligence." Elife **7**: e41714.

bioRxiv preprint doi: https://doi.org/10.1101/748988; this version posted August 29, 2019. The copyright holder for this preprint (which was not certified by peer review) is the author/funder, who has granted bioRxiv a license to display the preprint in perpetuity. It is made available under aCC-BY-NC-ND 4.0 International license.

Groppe, D. M., S. Bickel, C. J. Keller, S. K. Jain, S. T. Hwang, C. Harden and A. D. Mehta (2013). "Dominant frequencies of resting human brain activity as measured by the electrocorticogram." Neuroimage **79**: 223-233.

Habib, N., I. Avraham-Davidi, A. Basu, T. Burks, K. Shekhar, M. Hofree, S. R. Choudhury, F. Aguet, E. Gelfand and K. Ardlie (2017). "Massively parallel single-nucleus RNA-seq with DroNc-seq." Nature methods **14**(10): 955.

Higgs, M. H. and W. J. Spain (2009). "Conditional bursting enhances resonant firing in neocortical layer 2–3 pyramidal neurons." Journal of Neuroscience **29**(5): 1285-1299.

Hodge, R. D., T. E. Bakken, J. A. Miller, K. A. Smith, E. R. Barkan, L. T. Graybuck, J. L. Close, B. Long, O. Penn, Z. Yao, J. Eggermont, T. Hollt, B. P. Levi, S. I. Shehata, B. Aevermann, A. Beller, D. Bertagnolli, K. Brouner, T. Casper, C. Cobbs, R. Dalley, N. Dee, S.-L. Ding, R. G. Ellenbogen, O. Fong, E. Garren, J. Goldy, R. P. Gwinn, D. Hirschstein, C. D. Keene, M. Keshk, A. L. Ko, K. Lathia, A. Mahfouz, Z. Maltzer, M. McGraw, T. N. Nguyen, J. Nyhus, J. G. Ojemann, A. Oldre, S. Parry, S. Reynolds, C. Rimorin, N. V. Shapovalova, S. Somasundaram, A. Szafer, E. R. Thomsen, M. Tieu, R. H. Scheuermann, R. Yuste, S. M. Sunkin, B. Lelieveldt, D. Feng, L. Ng, A. Bernard, M. Hawrylycz, J. W. Phillips, B. Tasic, H. Zeng, A. R. Jones, C. Koch and E. S. Lein (2018). "Conserved cell types with divergent features between human and mouse cortex." bioRxiv: 384826.

Hu, H., K. Vervaeke and J. F. Storm (2002). "Two forms of electrical resonance at theta frequencies, generated by M-current, h-current and persistent Na+ current in rat hippocampal pyramidal cells." The Journal of physiology **545**(3): 783-805.

Hutcheon, B., R. M. Miura and E. Puil (1996). "Subthreshold membrane resonance in neocortical neurons." Journal of neurophysiology 76(2): 683-697.

Hutcheon, B. and Y. Yarom (2000). "Resonance, oscillation and the intrinsic frequency preferences of neurons." Trends in neurosciences 23(5): 216-222.

Kalmbach, B. E., A. Buchin, B. Long, J. Close, A. Nandi, J. A. Miller, T. E. Bakken, R. D. Hodge, P. Chong, R. de Frates, K. Dai, Z. Maltzer, P. R. Nicovich, C. D. Keene, L. Silbergeld, R. P. Gwinn, C. Cobbs, A. L. Ko, J. G. Ojemann, C. Koch, C. A. Anastassiou, E. S. Lein, J. T. Ting (2018). "h-Channels Contribute to Divergent Intrinsic Membrane Properties of Supragranular Pyramidal Neurons in Human versus Mouse Cerebral Cortex." Neuron 100(5): 1194-1208. e1195.

Köhling, R. and M. Avoli (2006). "Methodological approaches to exploring epileptic disorders in the human brain in vitro." Journal of neuroscience methods 155(1): 1-19.

Kostopoulos, G., C. Drapeau, M. Avoli, A. Olivier and J. G. Villemeure (1989). "Endogenous adenosine can reduce epileptiform activity in the human epileptogenic cortex maintained in vitro." Neuroscience letters 106(1): 119-124.

Lampl, I. and Y. Yarom (1997). "Subthreshold oscillations and resonant behavior: two manifestations of the same mechanism." Neuroscience **78**(2): 325-341.

Larsen, D. D., I. R. Wickersham and E. M. Callaway (2008). "Retrograde tracing with recombinant rabies virus reveals correlations between projection targets and dendritic architecture in layer 5 of mouse barrel cortex." Frontiers in neural circuits **2**: 5.

Mansouri, A., A. Fallah and T. A. Valiante (2012). "Determining surgical candidacy in temporal lobe epilepsy." Epilepsy research and treatment **2012**.

Markram, H., E. Muller, S. Ramaswamy, M. W. Reimann, M. Abdellah, C. A. Sanchez, A. Ailamaki, L. Alonso-Nanclares, N. Antille and S. Arsever (2015). "Reconstruction and simulation of neocortical microcircuitry." Cell **163**(2): 456-492.

McGinn, R. J. and T. A. Valiante (2014). "Phase–amplitude coupling and interlaminar synchrony are correlated in human neocortex." Journal of Neuroscience **34**(48): 15923-15930.

Migliore, M. and G. M. Shepherd (2005). "Opinion: an integrated approach to classifying neuronal phenotypes." Nature reviews. Neuroscience **6**(10): 810.

bioRxiv preprint doi: https://doi.org/10.1101/748988; this version posted August 29, 2019. The copyright holder for this preprint (which was not certified by peer review) is the author/funder, who has granted bioRxiv a license to display the preprint in perpetuity. It is made available under aCC-BY-NC-ND 4.0 International license.

Mohan, H., M. B. Verhoog, K. K. Doreswamy, G. Eyal, R. Aardse, B. N. Lodder, N. A. Goriounova, B. Asamoah, A. C. B. Brakspear and C. Groot (2015). "Dendritic and axonal architecture of individual pyramidal neurons across layers of adult human neocortex." Cerebral Cortex **25**(12): 4839-4853.

Molnár, G., S. Oláh, G. Komlósi, M. Füle, J. Szabadics, C. Varga, P. Barzó and G. Tamás (2008). "Complex events initiated by individual spikes in the human cerebral cortex." PLoS biology **6**(9): e222.

Neske, G. T. and B. W. Connors (2016). "Distinct roles of SOM and VIP Interneurons during Cortical up States." Frontiers in neural circuits **10**: 52.

Neuhoff, H., A. Neu, B. Liss and J. Roeper (2002). "Ih channels contribute to the different functional properties of identified dopaminergic subpopulations in the midbrain." Journal of Neuroscience **22**(4): 1290-1302.

Petersen, C. C., T. T. Hahn, M. Mehta, A. Grinvald and B. Sakmann (2003). "Interaction of sensory responses with spontaneous depolarization in layer 2/3 barrel cortex." Proceedings of the National Academy of Sciences **100**(23): 13638-13643.

Poulet, J. F. and C. C. Petersen (2008). "Internal brain state regulates membrane potential synchrony in barrel cortex of behaving mice." Nature **454**(7206): 881-885.

Puil, E., B. Gimbarzevsky and R. Miura (1986). "Quantification of membrane properties of trigeminal root ganglion neurons in guinea pigs." Journal of Neurophysiology **55**(5): 995-1016.

Robinson, R. B. and S. A. Siegelbaum (2003). "Hyperpolarization-activated cation currents: from molecules to physiological function." Annual review of physiology **65**(1): 453-480.

Ruzzo, E. K. and D. H. Geschwind (2016). "Schizophrenia genetics complements its mechanistic understanding." Nature Neuroscience **19**: 523.

Schmidt, S. L., C. R. Dorsett, A. K. Iyengar and F. Fröhlich (2016). "Interaction of intrinsic and synaptic currents mediate network resonance driven by layer V pyramidal cells." Cerebral Cortex **27**(9): 4396-4410.

Silva, G. T., M. B. Verhoog, N. B. Goriounova, A. Loebel, J. Hjorth, J. C. Baayen, C. P. De Kock and H. D. Mansvelder (2010). "Human synapses show a wide temporal window for spike-timing-dependent plasticity." Frontiers in synaptic neuroscience **2**: 12.

Silva, L. R., Y. Amitai and B. W. Connors (1991). "Intrinsic oscillations of neocortex generated by layer 5 pyramidal neurons." Science **251**(4992): 432-435.

Skinner, F. K. (2012). "Cellular-based modeling of oscillatory dynamics in brain networks." Current opinion in neurobiology **22**(4): 660-669.

Ting, J. T., T. L. Daigle, Q. Chen and G. Feng (2014). Acute brain slice methods for adult and aging animals: application of targeted patch clamp analysis and optogenetics. Patch-Clamp Methods and Protocols, Springer**:** 221-242.

Ulrich, D. (2002). "Dendritic resonance in rat neocortical pyramidal cells." Journal of neurophysiology **87**(6): 2753-2759.

Vigo, D. V., D. Kestel, K. Pendakur, G. Thornicroft and R. Atun (2019). "Disease burden and government spending on mental, neurological, and substance use disorders, and self-harm: cross-sectional, ecological study of health system response in the Americas." The Lancet Public Health **4**(2): e89-e96.

von Nicolai, C., G. Engler, A. Sharott, A. K. Engel, C. K. Moll and M. Siegel (2014). "Corticostriatal coordination through coherent phase-amplitude coupling." Journal of Neuroscience **34**(17): 5938-5948.

Womelsdorf, T., S. Ardid, S. Everling and T. A. Valiante (2014). "Burst firing synchronizes prefrontal and anterior cingulate cortex during attentional control." Current Biology **24**(22): 2613-2621.

Womelsdorf, T., T. A. Valiante, N. T. Sahin, K. J. Miller and P. Tiesinga (2014). "Dynamic circuit motifs underlying rhythmic gain control, gating and integration." Nature neuroscience **17**(8): 1031.

Yu, X. and E. R. Lewis (1989). "Studies with spike initiators: linearization by noise allows continuous signal modulation in neural networks." IEEE Transactions on Biomedical Engineering **36**(1): 36-43.

Zaitsev, A. V., N. V. Povysheva, G. Gonzalez-Burgos and D. A. Lewis (2012). "Electrophysiological classes of layer 2/3 pyramidal cells in monkey prefrontal cortex." Journal of neurophysiology **108**(2): 595-609.

bioRxiv preprint doi: https://doi.org/10.1101/748988; this version posted August 29, 2019. The copyright holder for this preprint (which was not certified by peer review) is the author/funder, who has granted bioRxiv a license to display the preprint in perpetuity. It is made available under aCC-BY-NC-ND 4.0 International license.

Zemankovics, R., S. Káli, O. Paulsen, T. F. Freund and N. Hájos (2010). "Differences in subthreshold resonance of hippocampal pyramidal cells and interneurons: the role of h-current and passive membrane characteristics." The Journal of physiology **588**(12): 2109-2132.